

Analysis of Flow and Heat Transfer in the U.S. EPR™ Heavy Reflector

Kohei Takamuku

Thesis submitted to the faculty of the Virginia Polytechnic Institute and State University
in partial fulfillment of the requirements for the degree of

Master of Science
In
Mechanical Engineering

Danesh K. Tafti – Chair
Tom E. Diller
Mark R. Paul

December 5, 2008
Blacksburg, VA

Keywords: CFD, Fluid Dynamics, Conjugate Heat Transfer, Nuclear, PWR,
Heavy Reflector, Turbulent Flow, Cooling Channels

Copyright 2008, Kohei Takamuku

Analysis of Flow and Heat Transfer in the U.S. EPR™ Heavy Reflector

Kohei Takamuku

ABSTRACT

The U.S. EPR™ Reactor is a new, large-scale pressurized water reactor designed by AREVA. Surrounding the core of this reactor is a steel wall structure called the heavy reflector. The purpose of the heavy reflector is to reduce the neutron flux escaping the core and thus increase the efficiency of the reactor while reducing the damage to the structures surrounding the core as well. The heavy reflector is heated due to absorption of the gamma radiation, and this heat is removed by the water flowing through 832 cooling channels drilled through the heavy reflector.

In this project, the temperature distribution in the heavy reflector was investigated to ascertain that the maximum temperature does not exceed the allowable temperature of 350 °C, with the intent of modifying the flow distribution in the cooling channels to alleviate any hot spots. The analysis was conducted in two steps. First, the flow distribution in the cooling channels was calculated to test for any maldistribution. The temperature distribution in the heavy reflector was then calculated by simulating the conjugate heat transfer with this flow distribution as the coolant input.

The turbulent nature of the flow through the cooling channels made the calculation of the flow distribution computationally expensive. In order to resolve this problem, a simplification method using the “equivalent flow resistance” was developed. The method was validated by conducting a few case studies. Using the simplified model, the flow distribution was calculated and found to be fairly uniform.

The conjugate heat transfer calculation was conducted. The same simplification method used in the flow distribution analysis could not be applied to this calculation; therefore, the computational cost of this model was reduced by lowering the grid density in the fluid region. The results showed that the maximum temperature in the heavy reflector is 347.7 °C, which is below the maximum allowable temperature of 350 °C. Additional studies were conducted to test the sensitivity of the maximum temperature with change in the flow distribution in the cooling channels. Through multiple calculations, the maximum temperature did not drop more than 3 °C; therefore, it was concluded that the flow distribution in the cooling channels does not have significant effect on the maximum temperature in the heavy reflector.

To the Lord God Almighty

Acknowledgement

This thesis is by far the greatest accomplishment in my academic career. There has been no other work that I have put as much effort or time as I did for this one. However, I cannot claim all the credit for the completion of this thesis. Over the year and a half that I have spent writing this thesis, I have received so much support from many people, either directly or indirectly. Without their support, this work would not be complete, and I would not be where I am.

First I would like to thank my advisor Dr. Danesh Tafti. Not only he made sure that my education was funded throughout my program, he always took time to give me guidance on my research work, motivated me to work, let me be flexible with my work schedule when needed, and showed me great amount of patience and understanding even when I made mistakes. Dr. Tafti, I was very blessed to have an advisor like you.

Thanks to my committee members Dr. Tom Diller and Dr. Mark Paul as well for taking their time to review my work and making suggestions for improvements. I have also taken courses with them and received valuable knowledge and experience.

I would also like to acknowledge the Center for Advanced Engineering and Research (CAER) for providing the funding for the project and AREVA, especially Matt Touna and Bernie Copsey, for providing all the information that was necessary to complete the project.

I am also grateful for my colleagues in the HPCFD lab: Shi-Ming Li, Ali Rozati, Pradeep Gopalakrishnan, Mohammad Elyyan, Sai Shrinivas, Naresh Selvarasu, Jose Tijiboy, Sunil Patil, Amit Amritkar, Jonathan Cowan, Nagendra Krishnamurthy, and Kamal Viswanath. Shi-Ming, thanks for getting me to join the Virginia Tech table tennis club. It was great to play in so many different tournaments. I even ended up going all the way to the college nationals with the team, and that was a great experience. Ali, Mohammad, and Sai, you three gave me many advices and supports, especially when I just came to this lab. Things would not have gone as smoothly as they did if it wasn't for you. Naresh, Jose, and Sunil, I have taken multiple courses with you guys and received so much help on the assignments. It is always good to have buddies who stay up late together to finish up the work.

I would also like to give many thanks to some of my best friends Jennifer Souder, Casey Mask, Thea Edwards, Kate Hooper, my brother Ronald Quilaton, my sister Amy Duncan, and many other friends from Lipscomb University. It is because of you that I was able to overcome the loneliness that I experienced at the beginning of my study here as well as some of the hardships that I faced during my stay at Blacksburg. You all gave me great amount of love and continued to encourage me throughout my study. I would not be where I am right now if you all were not there. I love you all.

Thanks also to my parents in Japan. It is because of them that I am in the U.S. and was able to receive such high level education. Thank you for all the supports, both financially and mentally.

Finally, my greatest thanks go to the God, my Lord. I thank you for all the great blessings that you give me. Thank you for such an opportunity to learn many valuable lessons, not only in academics but also in spiritual life. Thank you for all the people, events, and many other things that you put in my life. And most of all, thank you for the greatest love that only you can provide. May this work bring glory to your name.

TABLE OF CONTENTS

CHAPTER 1. INTRODUCTION	1
CHAPTER 2. FLOW DISTRIBUTION IN THE COOLING CHANNELS	5
2.1 Relevant Geometry.....	5
2.2 Material Properties and Operation Conditions.....	12
2.3 Flow Rates in the Heavy Reflector	12
2.4 Simplification of the Computational Model.....	14
2.4.1 Theory Behind the Method	14
2.4.2 Implementation of the Method in FLUENT	17
2.4.3 Case Studies for Validation	18
2.5 Calculation of Flow Distribution in the Heavy Reflector	23
2.6 Results	29
CHAPTER 3. TEMPERATURE DISTRIBUTION IN THE HEAVY REFLECTOR....	32
3.1 Relevant Geometry and Coolant Flows	32
3.2 Material Properties	33
3.3 Grid Sensitivity Study in the Coolant Flow Paths.....	34
3.3.1 Cooling Channels.....	35
3.3.2 Gap Around Tie Rod.....	39
3.3.3 Flow Inside the Tie Rod.....	42
3.3.4 Gap between the Heavy Reflector and the Core Barrel	44
3.3.5 Gap between the Heavy Reflector and the Vertical Key	48
3.4 Grid for the Heat Transfer Analysis.....	50
3.5 Implementation of Heat Source Data in FLUENT.....	53
3.6 Boundary Conditions.....	55
3.7 Results	59
3.8 Flow Rate Sensitivity Study.....	61
CHAPTER 4. SUMMARY AND CONCLUSION	63
References:	65
Appendix A Basic Equations.....	66
Appendix B Turbulence Model.....	67

Appendix C	Definition of Pressure in FLUENT.....	71
Appendix D	Determining K_o for the Orifices in the Heavy Reflector	72
Appendix E	Equations and Correlations for Grid Sensitivity Study	76
Appendix F	Data Format for Interpolation in FLUENT.....	78
Appendix G	MATLAB Code for Heat Generation Data Conversion	79
Appendix H	UDF Code from ANSYS Online Technical Support.....	82

LIST OF FIGURES

Figure 1.1: Power Generation Cycle in U.S. EPR [1]	1
Figure 1.2: Reactor Pressure Vessel [2].....	2
Figure 1.3: Heavy Reflector [2].....	4
Figure 2.1: Heavy Reflector [2].....	6
Figure 2.2: Heavy Reflector Cooling Channel [7].....	7
Figure 2.3: Top View of the Typical Slab [7].....	8
Figure 2.4: Schematic of the Lower Slab-Side View	10
Figure 2.5: Front View of the Inlets [6].....	10
Figure 2.6: Top View of the Lower Slab [6]	11
Figure 2.7: Simplified Schematic of a Heavy Reflector Cooling Channel.....	15
Figure 2.8: Outlet Vent Boundary Condition Panel in FLUENT	18
Figure 2.9: Schematic of Case 1	19
Figure 2.10: Plenum in Case 2.....	21
Figure 2.11: Two Different Channel Lengths used in Case 2.....	22
Figure 2.12: Top View/Schematic of Case 2	23
Figure 2.13: Computational Model for the Flow Distribution-Isometric View.....	25
Figure 2.14: Close Up View of the Plenum in Slab I	26
Figure 2.15: Mesh for the Cooling Channels-Top View	26
Figure 2.16: Computational Model for the Flow Distribution-Top View	27
Figure 2.17: Flow Distribution with $K_{eq} = 62.6$	29
Figure 2.18: Flow Distribution with $K_{eq} = 0$	31
Figure 3.1: Variables (a) Δy_1 and (b) Δx in Cooling Channels	36
Figure 3.2: Top View of the Tie Rod and the Associated Flow Paths.....	39
Figure 3.3: Isometric View of the Gap Around Tie Rod	40
Figure 3.4: Variables (a) Δy_1 and (b) Δx for the Gap Around Tie Rod.....	40
Figure 3.5: Overview of the Gap between the Heavy Reflector and the Core Barrel	45

Figure 3.6: Variables (1) Δy_1 , Δy_2 , and (2) Δx for Gap between the Heavy Reflector and the Core Barrel	45
Figure 3.7: Refinement of the Solid Region	51
Figure 3.8: Top View of the Heat Transfer Model	51
Figure 3.9: Isometric View of the Heat Transfer Model	52
Figure 3.10: Heat Generation due to Gamma Radiation (W/m^3).....	54
Figure.3.11: Inner Wall Free Stream Temperature Profile	57
Figure 3.12: The Curve Fit Equations Used to Implement the Temperature Profile in Figure 3.11 into FLUENT.....	58
Figure 3.13: Isometric View of the Temperature Distribution	60
Figure 3.14: Top View of the Temperature Distribution in Slab X.....	61
Figure 3.15: Temperature Distribution with 35 Channels without Orifices	62
Figure D.1: Orifice Grid	74

LIST OF TABLES

Table 2.1: Fluid Properties and Operation Conditions	12
Table 2.2: Minimum/Nominal/Maximum Bypass Flow Percentage Distribution [3]	13
Table 2.3: Case 1 Results.....	20
Table 2.4: Case 2 Results.....	23
Table 2.5: Solver Settings.....	28
Table 2.6: Inlet Conditions	28
Table 2.7: Outlet Conditions for Channel Outlets	28
Table 2.8: Flow to the Annulus.....	28
Table 2.9: Summary of the Flow Distribution with $K_{eq} = 62.6$	29
Table 2.10: Summary of Flow Distribution with $K_{eq} = 0$	31
Table 3.1: Water Properties	33
Table 3.2: Stainless Steel Properties.....	33
Table 3.3: Heat Transfer Coefficients for Cooling Channels ($\Delta y_1 = 0.1$ mm, $\Delta x = 1$ mm, and $N = 32$)	37
Table 3.4: Variation in Δy_1 and Resulting Heat Transfer Coefficients for Cooling Channels ($\Delta x/\Delta y_1 = 50$, $N = 16$).....	37
Table 3.5: Variation in Δx and Resulting Heat Transfer Coefficients for Cooling Channels ($\Delta y_1 = 0.5$ mm, $N = 16$)	38
Table 3.6: Variation in N and the Resulting Heat Transfer Coefficients for Cooling Channels ($\Delta y_1 = 0.5$ mm, $\Delta x = 15$ mm).....	38
Table 3.7: Heat Transfer Values in the Gap around the Tie Rod ($\Delta y_1 = 0.2$ mm, $\Delta x = 1$ mm, $N = 32$).....	41
Table 3.8: Variation in Δy_1 and Resulting Heat Transfer Coefficients with Percent Difference from the Initial Values for Gap around Tie Rod ($\Delta x = 1$ mm, $N = 32$).....	41
Table 3.9: Variation in Δx and Resulting Heat Transfer Coefficients with Percent Difference from the Initial Value for Gap around Tie Rod ($\Delta y_1 = 0.2$ mm, $N = 32$).....	42
Table 3.10: Variation in N and Resulting Heat Transfer Coefficients with Percent Difference from the Initial Value for Gap around Tie Rod ($\Delta y_1 = 0.2$ mm, $\Delta x = 1$ mm)	42

Table 3.11: Heat Transfer Coefficient Values in the Flow Inside Tie Rod ($\Delta y_1 = 0.2$ mm, $\Delta x = 1$ mm, $N = 32$)	43
Table 3.12: Variation in Δy_1 and Resulting Heat Transfer Coefficients with Percent Difference from the Initial Value for Flow Inside Tie Rod ($\Delta x = 15$ mm, $N = 16$)	44
Table 3.13: Reference Heat Transfer Values for Gap between the Heavy Reflector and the Core Barrel ($\Delta y_1 = 0.2$ mm, $\Delta y_2 = 1$ mm, $\Delta x = 1$ mm)	46
Table 3.14: Variation in Δy_1 and Resulting Heat Transfer Coefficients with Percent Difference from Initial Value for the Gap between the heavy Reflector and the Core Barrel ($\Delta y_2 = 1$ mm, $\Delta x = 1$ mm)	46
Table 3.15: Variation in Δy_2 and Resulting Heat Transfer Coefficients with Percent Difference from Initial Value for the Gap between the heavy Reflector and the Core Barrel ($\Delta y_1 = 0.2$ mm, $\Delta x = 1$ mm)	47
Table 3.16: Variation in Δx and Resulting Heat Transfer Coefficients with Percent Difference from Initial Value for the Gap between the heavy Reflector and the Core Barrel ($\Delta y_1 = 0.2$ mm, $\Delta y_2 = 1$ mm)	47
Table 3.17: Reference Heat Transfer Values for the Gap between the Heavy Reflector and the Vertical Key ($\Delta y_1 = 0.2$ mm, $\Delta y_2 = 0.2$ mm, $\Delta x = 1$ mm).....	49
Table 3.18: Variation in Δy_1 and Resulting Heat Transfer Coefficients with Percent Difference from Initial Value for the Gap between the heavy Reflector and the Vertical Key ($\Delta y_2 = 0.2$ mm, $\Delta x = 15$ mm).....	49
Table 3.19: Variation in Δy_2 and Resulting Heat Transfer Coefficients with Percent Difference from Initial Value for the Gap between the heavy Reflector and the Vertical Key ($\Delta y_1 = 0.2$ mm, $\Delta x = 15$ mm).....	50
Table 3.20: Mass Flow Inlets.....	56
Table 3.21: Velocity Inlets.....	56
Table 3.22: Inlet Temperature.....	56
Table 3.23: Wall Boundary Conditions	56
Table D.1: K Value for an Orifice	75

CHAPTER 1. INTRODUCTION

The use of nuclear energy for power generation is once again gaining prominence in light of the increasing costs and environmental concerns associated with burning fossil fuels. One of the newer designs of a nuclear power generator that achieves safety and efficiency is the U.S. EPR™ pressurized water reactor (PWR), designed by AREVA. The heat generated in the core through chain reactions of nuclear fuel is transferred to the primary fluid, which, in this case, is pressurized water to avoid boiling. The pressurized high temperature water is then used to generate steam in a secondary loop to drive the turbine for power generation. Figure 1.1 shows the schematic of the U.S. EPR™ PWR.

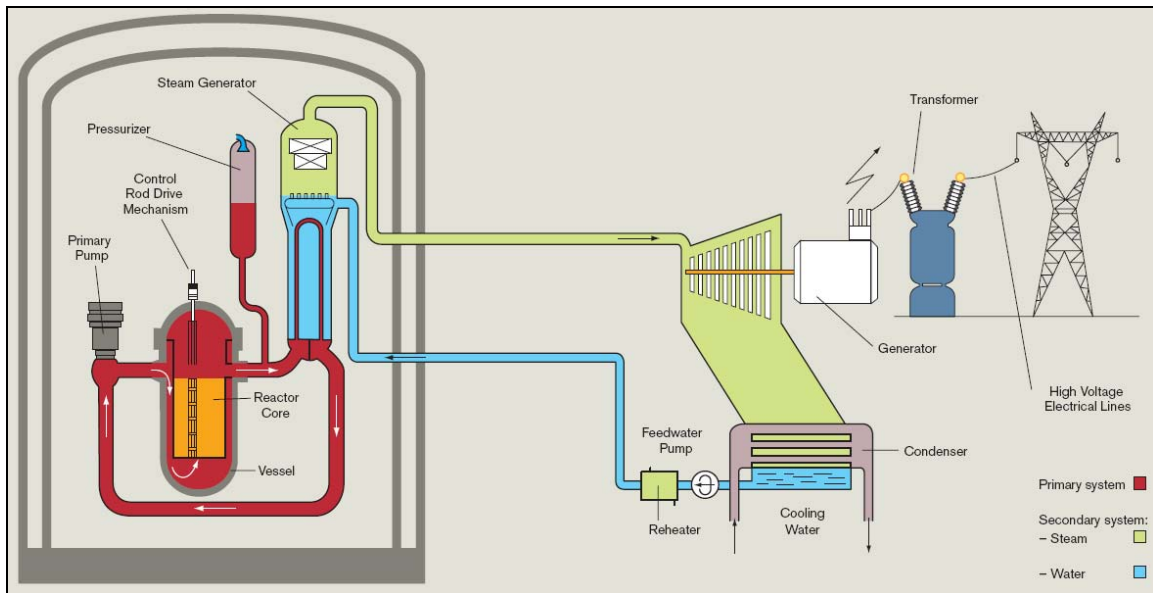


Figure 1.1: Power Generation Cycle in U.S. EPR™ Reactor [1]

The core of the reactor is located inside a vessel called the reactor pressure vessel. The reactor pressure vessel has various components to control and contain the nuclear reactions in the core. The thermal power of the core is about 4590 MWth. The water flows into the vessel through its inlets with an average temperature of 295 °C. It then goes through a distribution plenum at the bottom of the vessel into the core, gains heat through

cooling of the fuel assemblies as well as absorption of neutrons, and exits to the steam generator with a nominal temperature of 330 °C.

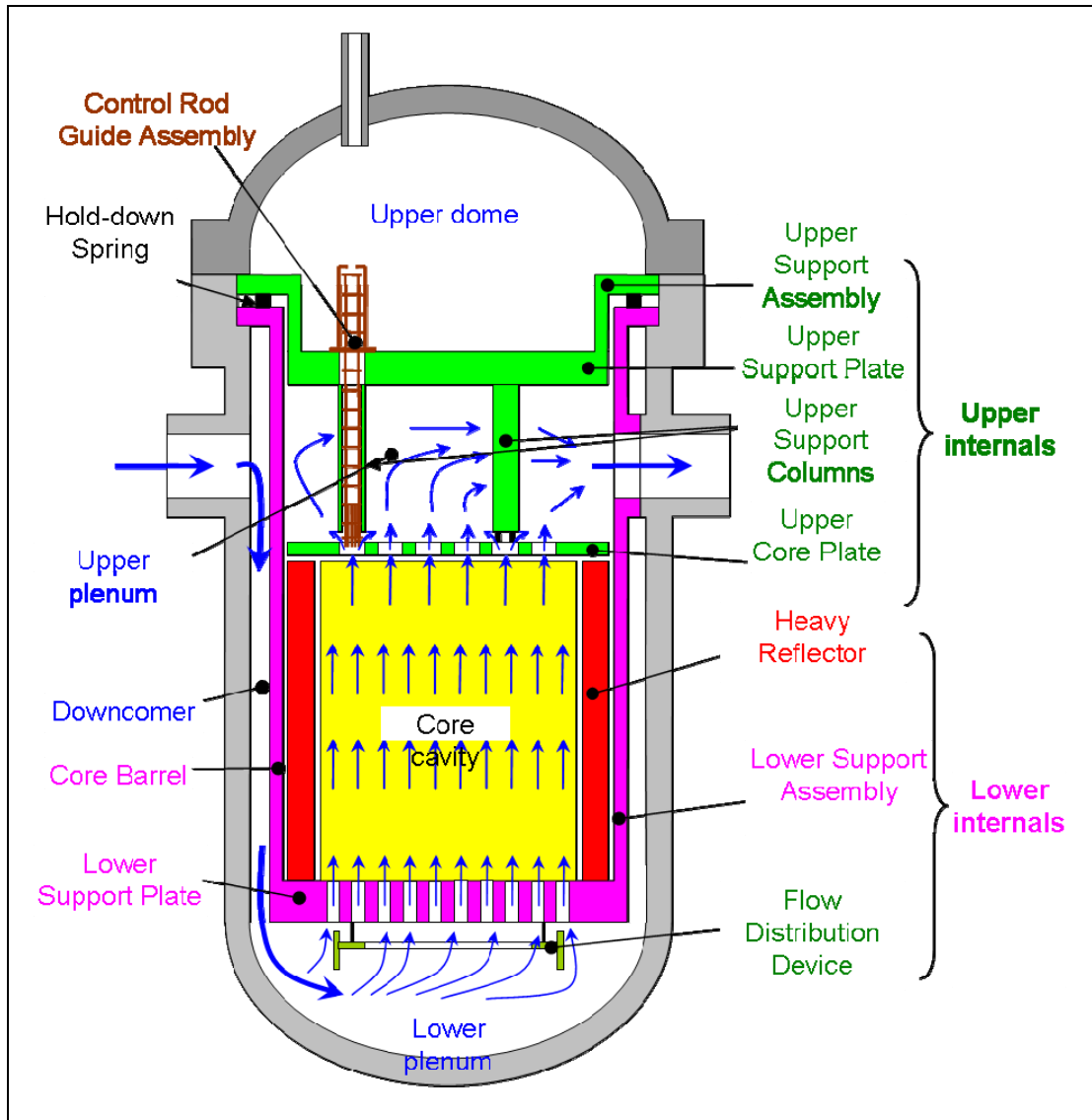


Figure 1.2: Reactor Pressure Vessel [2]

One of the aspects in the U.S. EPR™ reactor that makes this design different from other PWRs is a structure that sits inside the reactor vessel called the heavy reflector, shown in Figure 1.3. The heavy reflector is a wall made of 12 stainless steel slabs stacked vertically surrounding the reactor core. Some of the benefits of using the heavy reflector include reducing neutron leakage from the core, which protects the reactor vessel from neutron damage and increases the efficiency of fuel usage. While acting as a shield, the

heavy reflector is heated due to absorption of the gamma radiation. In order to avoid overheating, the heat in the reflector is removed by water flowing through 832 cooling channels drilled through the reflector, shown as small dots at the top of the reflector in Figure 1.3. Each channel is 13 mm in diameter with a number of orifices, which are used to calibrate the flow in each channel by varying the resistance. The bottom slab of the reflector has a plenum inside it and acts as a distribution chamber. A small portion of the water flowing through the core is taken into this plenum through small inlets at the bottom of the reflector. From the plenum, the majority of the water flows into the cooling channels while a small percentage of it flows into the gap between the reflector and the inner wall of the core barrel, which is a wall that acts as the container for the core and various internal structures. There are also eight tie rods that keep the reflector in place. These tie rods also have flow inside to provide additional cooling for the reflector. The flow inside the tie rods is provided from their own inlets that are set outside the core barrel and is separate from the flow in the reflector. There are also small gaps between the reflector and various structural parts, including the tie rods, where some of the water flows through. All of these flows exit at the top of the reflector and eventually merge back to the core main stream.

The objective of this thesis is to conduct a computational fluid dynamics (CFD) analysis to calculate the temperature distribution in the heavy reflector slabs to ascertain that the maximum temperature does not exceed the allowable temperature of 350 °C, with the intent of modifying the flow distribution in the cooling channels to alleviate any hot spots. To perform the heat transfer analysis, the first task is to calculate the correct flow distribution in the cooling channels from the plenum to test for any maldistribution. The calculated flow distribution is then used to perform a conjugate heat transfer analysis in the heavy reflector.

In Chapter 2, the distribution of the water among the cooling channels is calculated. Chapter 3 uses the flow distribution found in Chapter 2 to conduct the heat transfer analysis to find the temperature distribution in the heavy reflector. Finally, Chapter 4 presents the summary and the conclusions from the analysis.

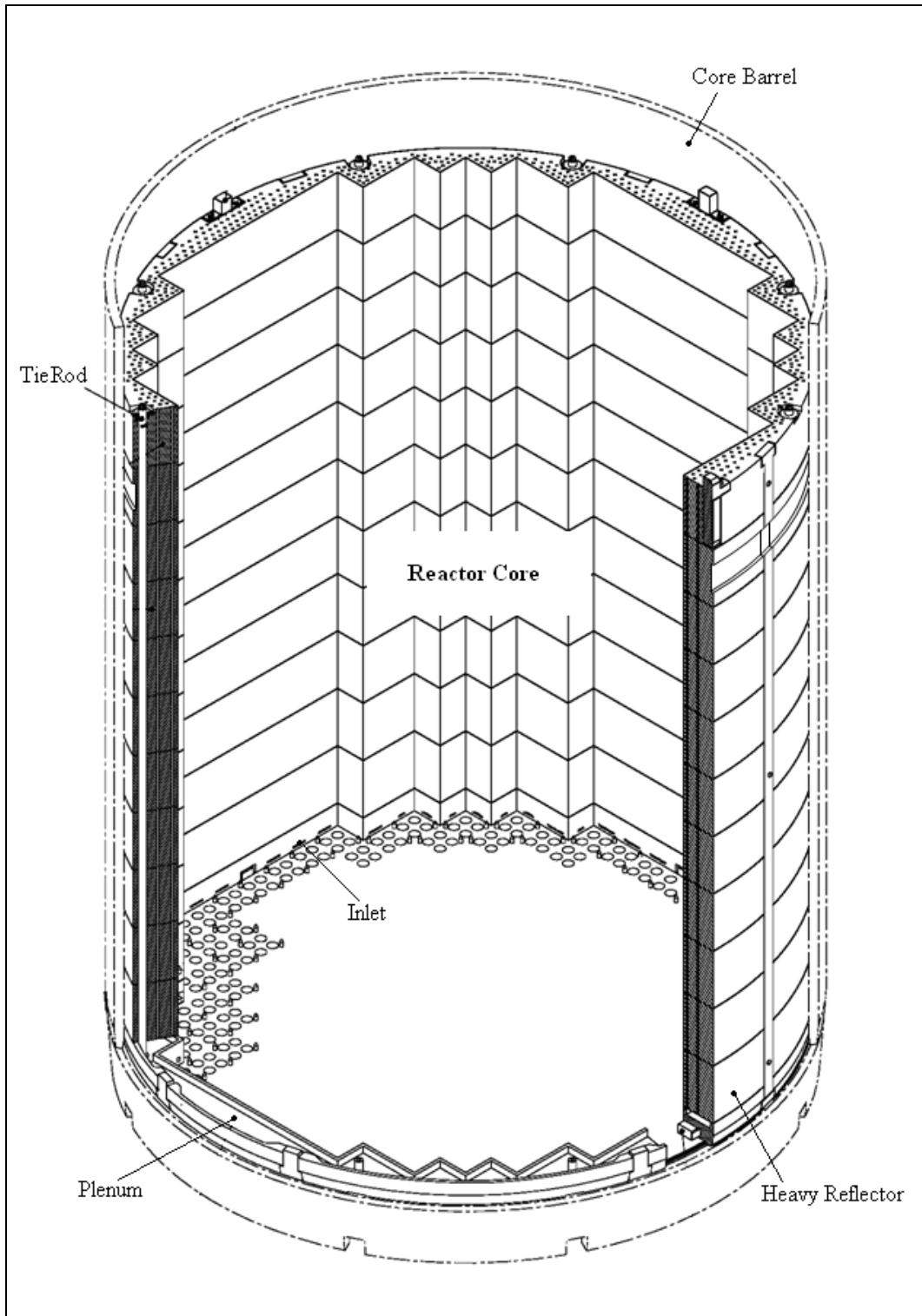


Figure 1.3: Heavy Reflector [2]

CHAPTER 2. FLOW DISTRIBUTION IN THE COOLING CHANNELS

In this chapter, the flow distribution among the cooling channels in the heavy reflector is calculated so that the correct flow rates can be used for the conjugate heat transfer calculation in the next chapter. The total flow rate into the heavy reflector and the cooling channels is given by AREVA. from their previous study on the hydraulics in the heavy reflector [3]. The flow rates in the individual cooling channels and their variation is to be investigated based on this given data. The chapter proceeds in the following manner: description of the geometry that is relevant to the calculation, a list of material properties and operation conditions, detail of the given data and the estimated average flow rate per channel, derivation and validation of the simplification methodology used in the calculation, description of the computational model, and finally the results.

2.1 Relevant Geometry

The general structure of the heavy reflector is shown in Figure 2.1. The heavy reflector consists of twelve stainless steel slabs stacked together, axially restrained by vertical keys and tie rods, with a small gap between their outer diameter and the inner wall of the core barrel. This gap is called the annular region. Eleven slabs on the top, called slabs II through XII, are almost all identical with 417 mm height except the top slab, Slab XII, having a slightly larger diameter, 4160 mm instead of 4156 mm, and the one below, Slab XI, having a 20 mm groove on its outer diameter. Slabs II through X are also known as Typical Slabs.

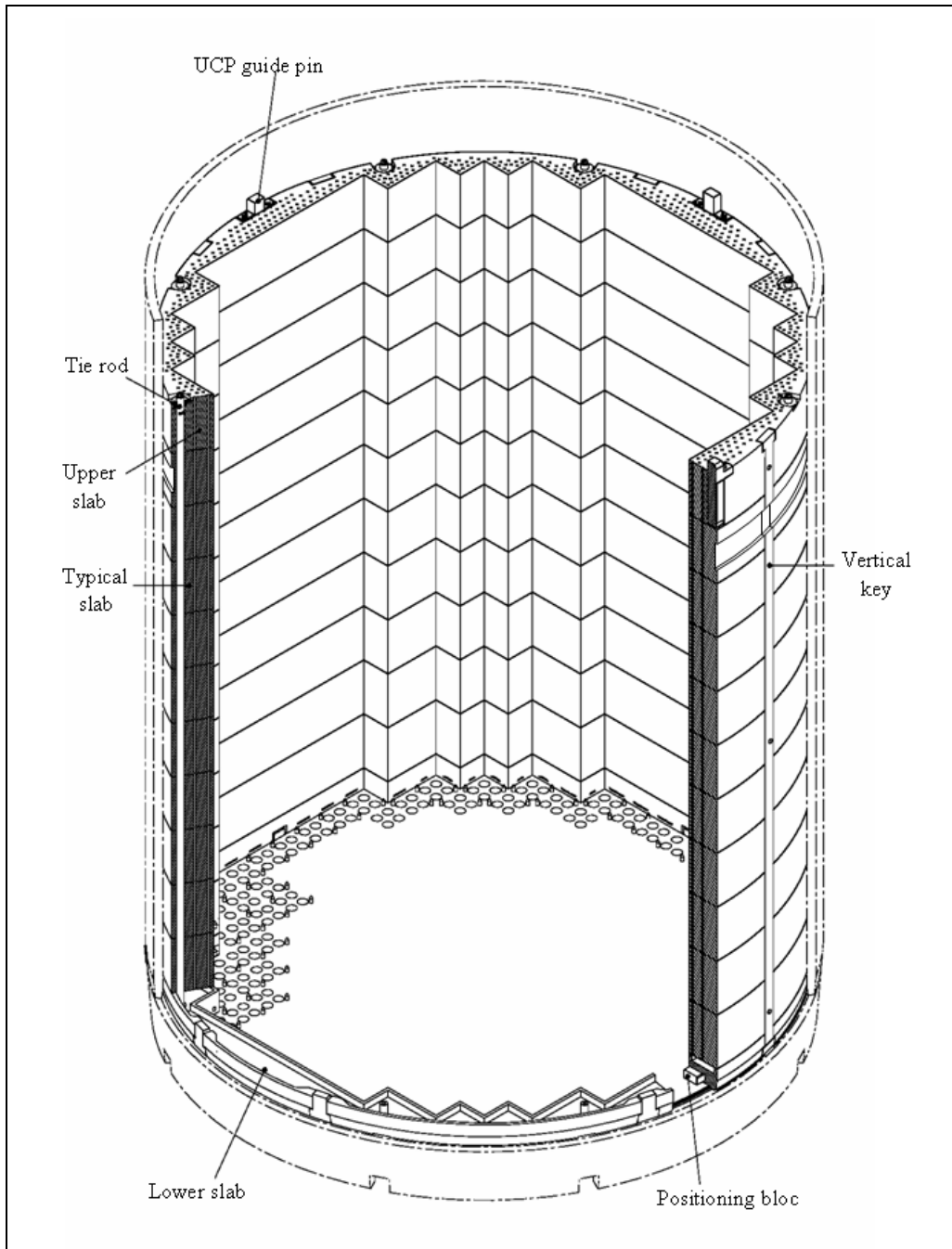


Figure 2.1: Heavy Reflector [2]

Each slab has 832 cooling channels with 13 mm diameter drilled through for the water to flow. All cooling channels are identical to each other, with each having an 8 mm diameter orifice at the bottom of each slab to calibrate the flow among the channels. The detailed sketch of a cooling channel is shown below, and the distribution of the cooling channels for 1/8 of the Typical Slab is shown in Figure 2.3 on the next page.

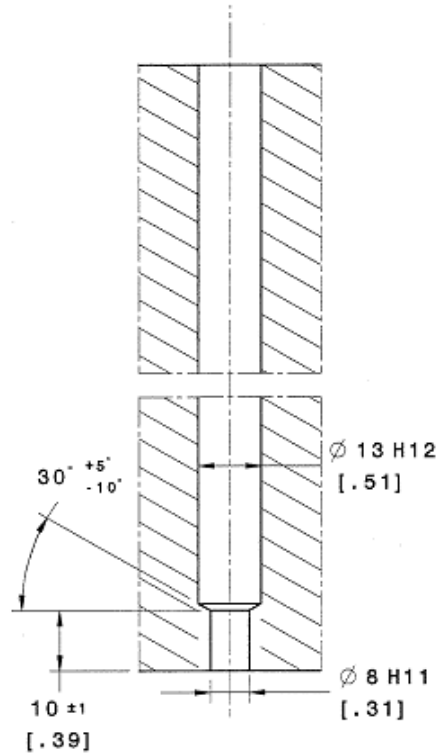


Figure 2.2: Heavy Reflector Cooling Channel [7]

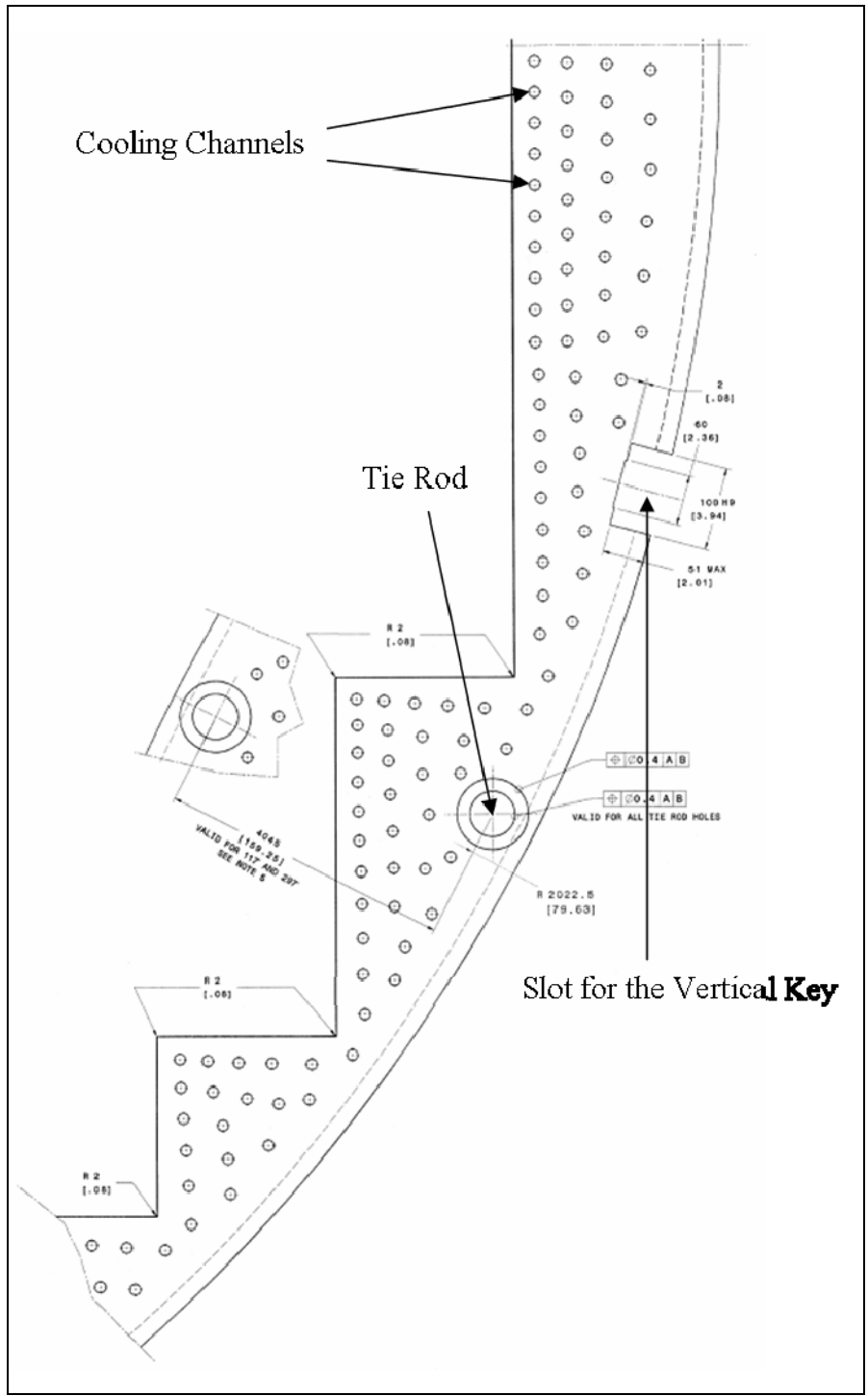


Figure 2.3: Top View of the Typical Slab [7]

The slab at the very bottom, called Lower Slab or Slab I, consists of a plenum, or the distribution channel as labeled in Figure 2.4 on the next page, 56 inlets at the bottom, and holes distributed close to equally spaced around its outer wall to let some of the water flow out to the annular region. All inlets consist of a number of small holes facing the core and a vertical space between those holes and the plenum. Some inlets are wider than the others and have 21 of those small holes while the others have 11, as shown in Figure 2.5. The flow is distributed among the cooling channels in Slab II sitting on top of Slab I as well as other flow paths such as gaps between the heavy reflector and various structures, such as the vertical keys and the tie rods. Figures 2.4 through 2.6, show the flow process in the lower slab from the side, the front view of the inlets facing the core, and the top view of Slab I, respectively. More detailed drawings of the slabs including their dimensions, channel locations, and structures are included in [5], [6], and [7].

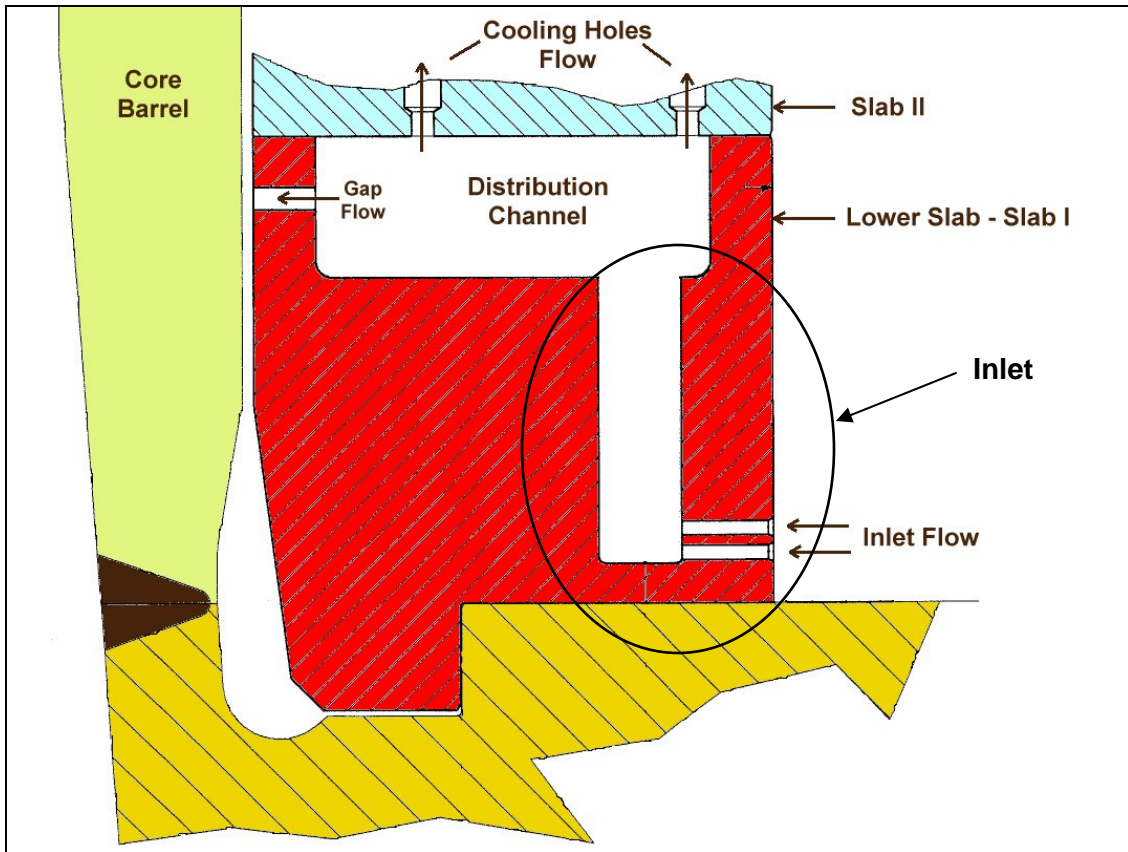


Figure 2.4: Schematic of the Lower Slab-Side View
 Courtesy AREVA

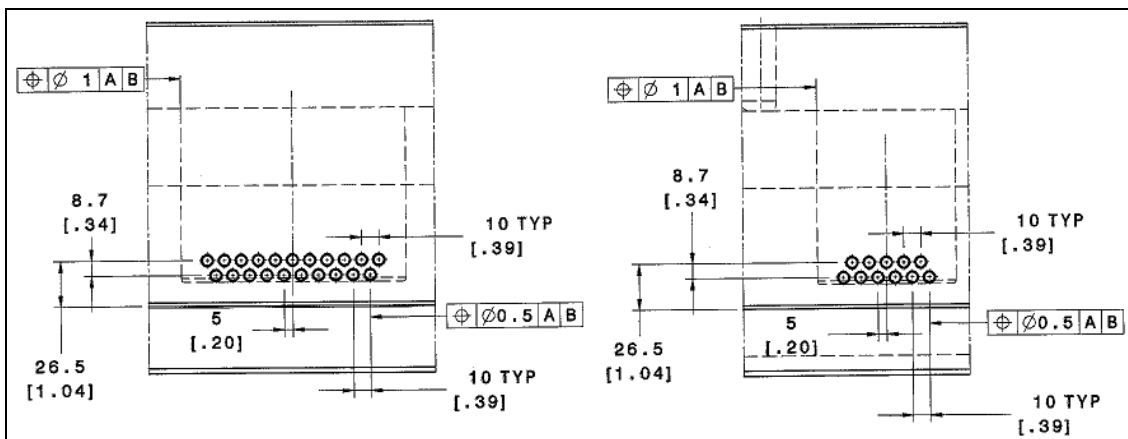


Figure 2.5: Front View of the Inlets [6]

2.2 Material Properties and Operation Conditions

The fluid properties are calculated based on the water properties under the condition, 315 °C and 15.51 million Pa, and are listed in Table 2.1 below. 315 °C is chosen because it is about midway of the nominal inlet and outlet temperatures of the reactor core, 295 °C and 330 °C, found in Reference [1]. Change in the fluid temperature within this range does not affect the fluid properties by much because the water is highly pressurized. For this reason, the properties of the water are assumed to be constant throughout the calculation. 15.51 million Pa is the pressure at which the system is maintained [1].

Table 2.1: Fluid Properties and Operation Conditions

Density (kg/m ³)	691.9
Viscosity (kg/m-s)	0.00008241
Operation Pressure (Pa)	1.551 x 10 ⁷
Operation Density (kg/s)	0
Gravity (m/s ²)	9.81

2.3 Flow Rates in the Heavy Reflector

The pressurized water that goes through the reactor core and transfers heat to the steam generator is also known the primary coolant. This primary coolant keeps running in a loop using a pump called reactor coolant pump (RCP). This loop is called the reactor coolant system (RCS), and its flow rates are called RCS flow rates. Since the bypass flow through the heavy reflector is provided from this RCS flow through the core, the inlet flow rate for the heavy reflector can be calculated based on this flow rate. In Reference [3], there are three different RCS flow rates listed: thermal-hydraulic design, nominal, and mechanical design flow rates. Thermal-hydraulic design and mechanical design flow rates are the lower and the upper limits based on the nominal flow rate and its uncertainty, which is determined through experiments. Reference [3] also lists the

percentage distribution of the flow in the heavy reflector as shown in Table 2.2 for minimum, nominal, and maximum bypass flow conditions. Again the minimum and the maximum bypass flows are determined based on the uncertainty of the nominal flow rate. For the purpose of this report, the combination of thermal-hydraulic RCS flow rate, involving four coolant pumps with 27,185 m³/hr each, and the minimum bypass flow is used since it is the most conservative scenario for the heat transfer analysis. The amount of flow through the gap between the heavy reflector and the tie rod is assumed to be negligible for the purpose of calculating the flow distribution among the cooling channels.

Table 2.2: Minimum/Nominal/Maximum Bypass Flow Percentage Distribution [3]

Path	Minimum	Nominal	Maximum
Spray Nozzles	0.33%	0.36%	0.39%
Hot Leg Gap	0%	0.26%	1.04%
Baffle Face Flow	0%	0.13%	0.18%
Heavy Reflector Flow	--	--	--
Into Vert HR Holes	0.77%	0.80%	0.81%
Assumed Core to HR holes thru HR Gaps	0%	0.04%	0.06%
Barrel Gap	0.16%	0.18%	0.19%
Around/Thru Tie Rods	0.02%	0.02%	0.03%
Tot Reflector flow	0.96%	1.04%	1.09%
Thimble Flows	--	--	--
3521 Plugged Thimbles	0.81%	0.99%	1.17%
75 Source Thimbles	0.02%	0.02%	0.02%
2136 CR Thimbles	0.92%	0.99%	1.20%
52 Instrument Thimbles (Sec. 5.2.1)	0.01%	0.01%	0.01%
Total Thimble Flow	1.75%	2.01%	2.40%
Total Bypass	3.04%	3.81%	5.11%

The total amount of water that comes into the heavy reflector for this calculation is determined by taking the sum of the percentages of the flow through the heavy reflector channels, 0.77%, and the flow into the annulus, 0.16%, which is total of 0.93% of the RCS flow rate. Note that the inlet flow is split among 56 inlets, some larger than the others and have more holes between the inlet and the core, as shown in Figure 2.3 in the previous section. The individual flow rates through the larger and the smaller inlets are calculated based on the number of holes connecting the flow from the core to the heavy reflector, with the assumption that each hole has the same amount of flow. Larger

inlets have 21 holes, and the smaller ones have 11; therefore, there are total of 936 of these holes. The total amount of flow into the heavy reflector is distributed equally among these holes. With this condition, the mass flow for the large and the small inlets are determined to be 4.408 kg/s and 2.309 kg/s, respectively. The flow into the annular region is also assumed to be distributed uniformly among the holes connecting the flow from the plenum and the annular region, which turns out to be 0.418 kg/s per hole. The average flow rate per cooling channel is 0.196 kg/s, which gives the average Reynolds number in the cooling channels of about 230,000.

2.4 Simplification of the Computational Model

In this section, a method of simplification for the computational model used for the flow distribution calculation is discussed. An ideal way is to model the entire heavy reflector and its flow paths to calculate the flow field. However, calculating the turbulent flow in the plenum and the cooling channels accurately require the mesh to be very fine. With 832 high aspect ratio cooling channels, modeling the entire reflector would be computationally too expensive. For this reason, the model has to be simplified so that the number of cells involved in the calculation would be more reasonable. In this calculation, there are two methods of simplification that are used. One is to use the fact that the geometry is symmetric and model only 1/8 of the original size. The other method is the use of equivalent flow resistance. The theory behind this method, the way to implement the method in FLUENT, and validations are discussed in the following three subsections.

2.4.1 Theory Behind the Method

The non-uniformity in the flow distribution among different flow paths is caused by the difference in the flow resistance. For example, the cooling channels that are close to the inlet are expected to have more flow than the ones farther away because the fluid has to flow through a longer distance, which means more flow resistance due to wall friction. The idea behind this method is to model just a part of the total length of the

cooling channels by putting an equivalent amount of flow resistance on them so that the resulting flow distribution would not be affected. The flow resistance of a flow path is measured in terms of the pressure drop; hence, the goal here is to make an environment where the pressure drop associated with the partial length of the cooling channel that is modeled is the same as that of the total length. This can be accomplished by using an outlet condition with loss coefficient. First, let us consider a single cooling channel. Here is a simplified schematic of a channel.

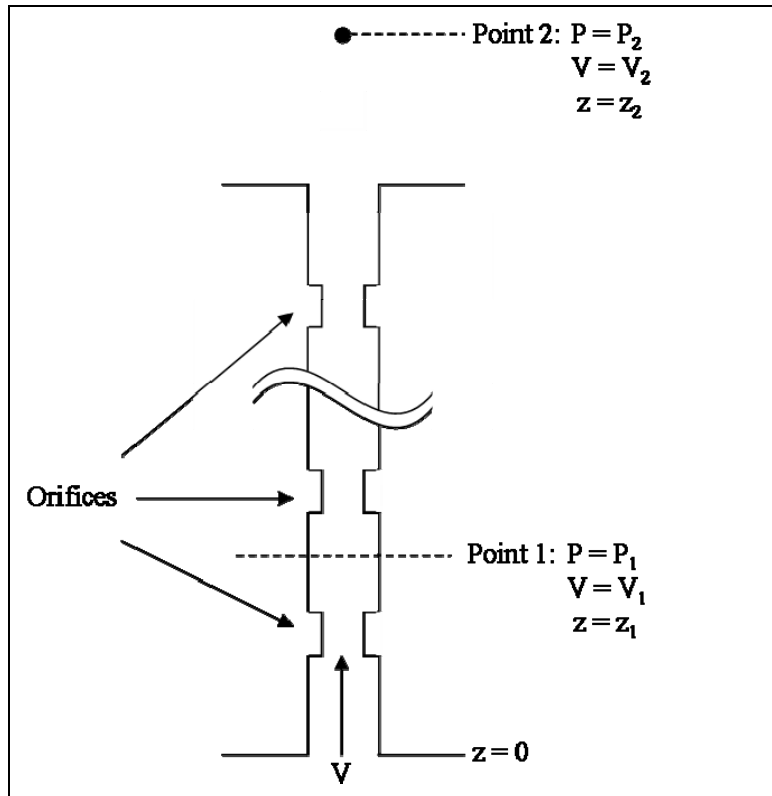


Figure 2.7: Simplified Schematic of a Heavy Reflector Cooling Channel

In the figure, P is the pressure, V is the average velocity, and z is the height. The partial length of the channel that is modeled is from the bottom of the channel to Point 1, some height z_1 above the inlet of the channel. Point 2 is some point above the outlet of the channel where the flow has expanded and the velocity has slowed down. The equation governing the pressure drop between the points 1 and 2 is

$$\frac{P_1}{\rho g} + \frac{V_1^2}{2g} + z_1 = \frac{P_2}{\rho g} + \frac{V_2^2}{2g} + z_2 + h_m + h_f \quad (2.1)$$

where ρ is the density, g is the gravity 9.81 m/s^2 , h_m is the head losses due to obstructions, such as the orifices, and h_f is the head loss due to friction, respectively. Since the velocity at Point 2 is very small, V_2 can be neglected. Also, it is assumed that the distance from the outlet of the channel to point 2 is not long; therefore, the height z_2 is assumed to be about the same height as the outlet of the channel. P_2 is assumed to be the same for every channel. The equation for h_m and h_f are the followings:

$$h_m = K_o \frac{V_1^2}{2g} + K_e \frac{V_1^2}{2g} \quad (2.2)$$

$$h_f = f \left(\frac{z_2 - z_1}{D} \right) \frac{V_1^2}{2g} \quad (2.3)$$

where K_o is the loss coefficient for the orifices, K_e is the loss coefficient for sudden expansion at the outlet, f is the Darcy friction coefficient, and D is the hydraulic diameter of the flow path. The flow is expanded into a very wide space at the outlet; therefore, the value of K_e becomes 1, according to Reference [4]. Substituting into and rearranging Equation (2.1), the pressure drop becomes

$$\begin{aligned} P_1 - P_2 = \Delta P &= -\frac{1}{2} \rho V_1^2 + \rho g(z_2 - z_1) + \rho g \left[K_o \frac{V_1^2}{2g} + K_e \frac{V_1^2}{2g} + f \left(\frac{z_2 - z_1}{D} \right) \frac{V_1^2}{2g} \right] \\ \Rightarrow \Delta P &= \rho g(z_2 - z_1) + \rho g \left[K_o \frac{V_1^2}{2g} + f \left(\frac{z_2 - z_1}{D} \right) \frac{V_1^2}{2g} \right] \end{aligned} \quad (2.4).$$

Note that the first term represents the pressure drop due to gravity, and the second term represents that due to head losses. Let them be called ΔP_g and ΔP_h , respectively. ΔP_g is a constant since all the values in this term are constants. ΔP_h , on the other hand, is velocity dependent. The equation for ΔP_h is the following.

$$\Delta P_h = \frac{1}{2} K_o \rho V^2 + \frac{1}{2} f \left(\frac{z_2 - z_1}{D} \right) \rho V^2 \quad (2.5).$$

Notice that both terms have common characteristics. They are both some constant values times the velocity squared. For this reason, it is possible to combine these terms into one term:

$$\Delta P_h = K_{eq} \frac{1}{2} \rho V^2 \quad \text{or} \quad \frac{\Delta P_h}{\rho g} = K_{eq} \frac{V^2}{2g} \quad (2.6)$$

where
$$K_{eq} = K_o + f \left(\frac{z_2 - z_1}{D} \right) \quad (2.7)$$

This form is the same form as the equation for a sudden expansion. Note that the friction factor f is normally dependent on the Reynolds number. However, the value of f does not vary too much within the expected range of Reynolds number in the cooling channels. Therefore, a constant value of f corresponding to the average Reynolds number per channel can be used, and K_{eq} also becomes constant. This value of f is about 0.015. If the channels are modeled up to the length z_1 with a sudden expansion at the outlet with the loss coefficient K_{eq} , the channels achieve the pressure drop that is the same as that of a channel with length z_2 . This sudden expansion at the outlet then represents the “equivalent resistance” of the flow path.

2.4.2 Implementation of the Method in FLUENT

In FLUENT, the sudden expansion at the outlet is represented with an outlet condition called Outlet Vent. The control panel for Outlet Vent condition is shown in Figure 2.8 below. This boundary condition is the same as the pressure outlet condition except it lets the user define a loss coefficient for any velocity-dependent pressure drop. FLUENT calculates the velocity-dependent term in Equation (2.6) based on the fluid velocity and the inputted loss coefficient value, K_{eq} . The pressure at the outlet is then determined by adding the resulting pressure drop to the gauge pressure specified by the user in the control panel.

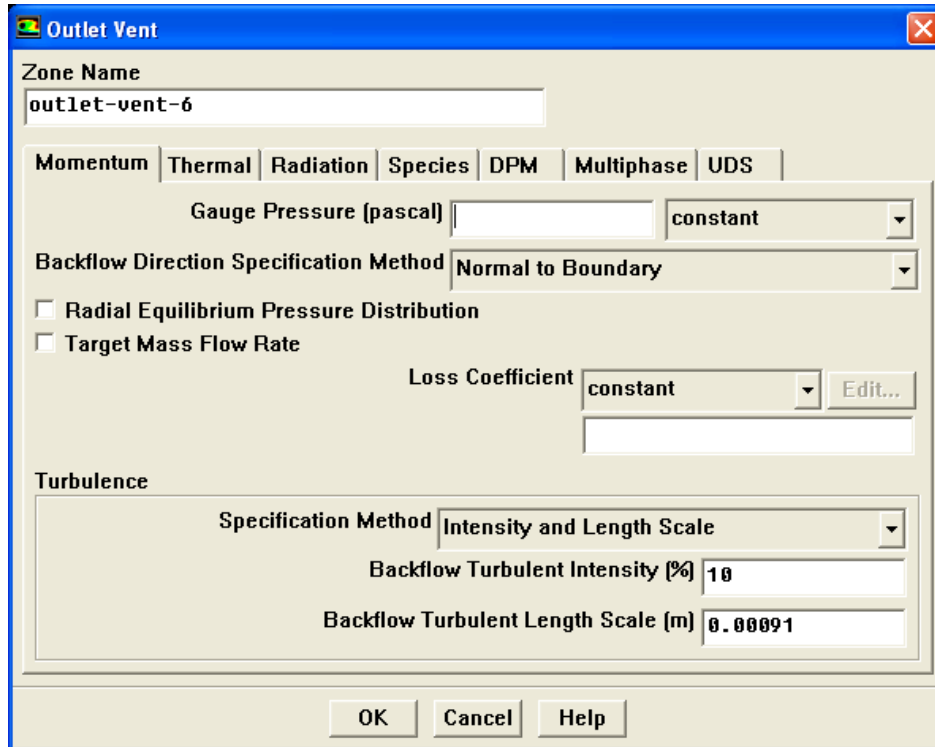


Figure 2.8: Outlet Vent Boundary Condition Panel in FLUENT

2.4.3 Case Studies for Validation

Two different case studies are conducted to validate the simplification method using the outlet vent condition. The first case, Case 1, involves a single channel with no orifice. The second case, Case 2, involves four channels.

The purpose of Case 1 is to show that the outlet vent can indeed represent an equivalent pressure drop, thus an equivalent resistance, for a given length of a channel without modeling the entire length. Two vertical channels are analyzed: channel 1 with an arbitrary length z_2 , and channel 2 with a shorter length z_1 with the outlet vent boundary condition at its outlet. Note that although the lengths of the channels are arbitrary, they have to be long enough for the flow to be fully-developed in order to accurately analyze the flow field because the friction factor used in calculation of K_{eq} is for the fully developed region. The schematic of this experiment is shown in Figure 2.9 in the next page.

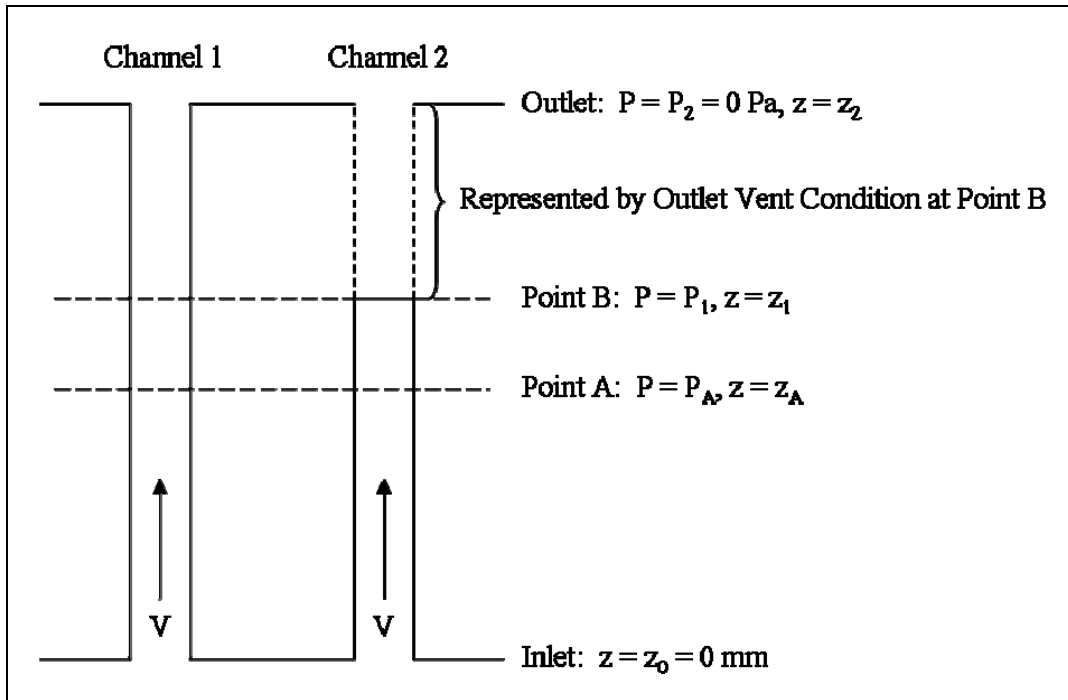


Figure 2.9: Schematic of Case 1

Point A is a point some length z_A away from the inlet where the flow is fully developed. The inlet flow rate is set to be the estimated average mass flow rate per channel discussed in section 2.3, and the pressure at the outlet of the channel 1, P_2 , is set to zero. The pressure at point A should be the same for both channels if the outlet vent condition in channel 2 successfully represents the pressure drop associated with the difference in length between the channels, which is calculated with Equation (2.4). The hydrostatic pressure drop term is calculated and input as the gauge pressure. This way, the hydrostatic pressure drop is added to the resulting pressure at the outlet of channel 2, which is denoted as point B in the figure. K_{eq} is calculated using Equation (2.7). Since these channels do not have any orifices, K_o is zero. With these settings, the flow field for each channel is computed, and the pressure at point A is compared. The results are shown in Table 2.3 in the next page.

Table 2.3: Case 1 Results

z_A (mm)	200
z_1 (mm)	300
z_2 (mm)	600
Inlet Mass Flow Rate (kg/s)	0.196
Pressure at Point A in Channel 1 (Pa)	3514
Gauge Pressure Set for the Outlet Vent in Channel 2 (Pa)	2036
K_{eq} for the Outlet Vent in Channel 2 (constant)	0.346
Pressure at Point A in Channel 2 (Pa)	3496
% Difference (%)	0.53

As shown in the table, the resulting pressures at point A for these two channels are in excellent agreement with each other. This shows that outlet vent condition successfully represents the equivalent pressure drop for the difference in the length between the channels.

Case 2 is similar to Case 1, but with four channels instead of just one. The calculation model consists of a randomly shaped plenum with four channels. In this case, the flow distribution in terms of mass flow at each outlet is investigated instead of the pressure drop in individual channel. The purpose of this study is to show that the flow distribution is not affected by shortening the channels using the outlet vent condition to represent the shortened length. The mesh for the plenum is shown in Figure 2.10 in the next page.

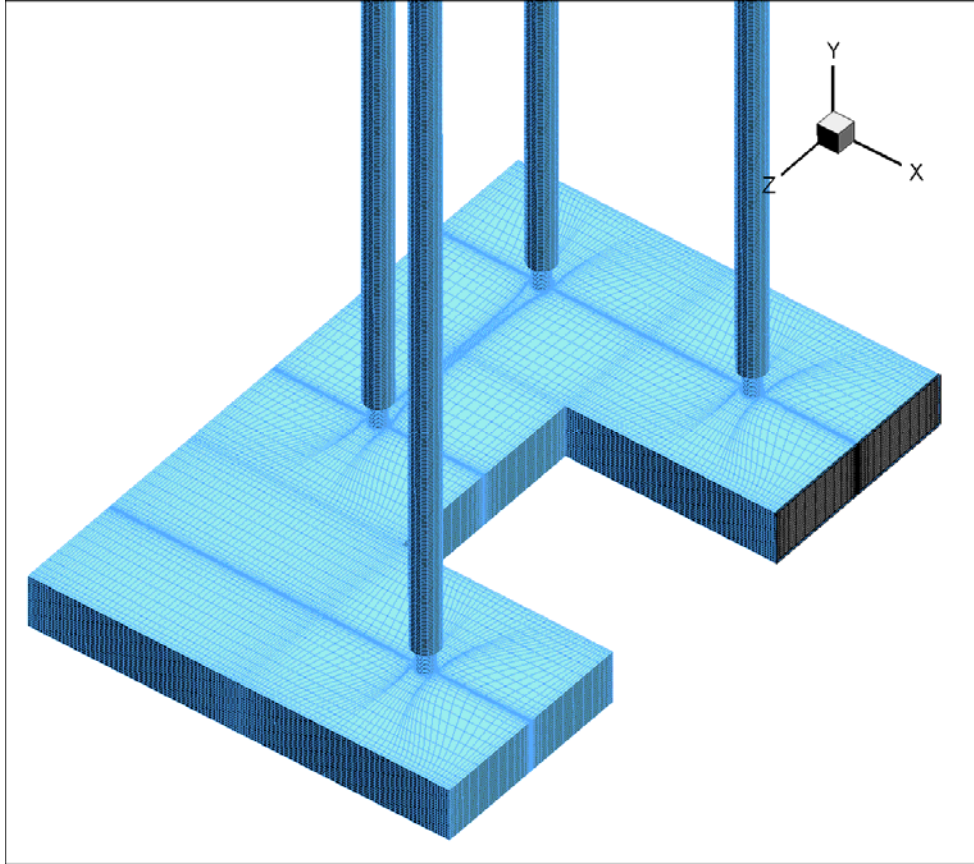


Figure 2.10: Plenum in Case 2

Just like Case 1, the flow field is calculated for two different models, one with long channels and another with shorter channels. The values needed for the outlet vent condition for the model with shorter channels are determined using the same procedure as Case 1, using Equation (2.5) for K_{eq} . Figure 2.11 and 2.12 in the following pages show the isometric and the top view of the models. The results are shown in Table 2.4 under Figure 2.12. The resulting flow distributions are in excellent agreement. The flow distribution is not affected by replacing an arbitrary length of the channels with the outlet vent boundary condition.

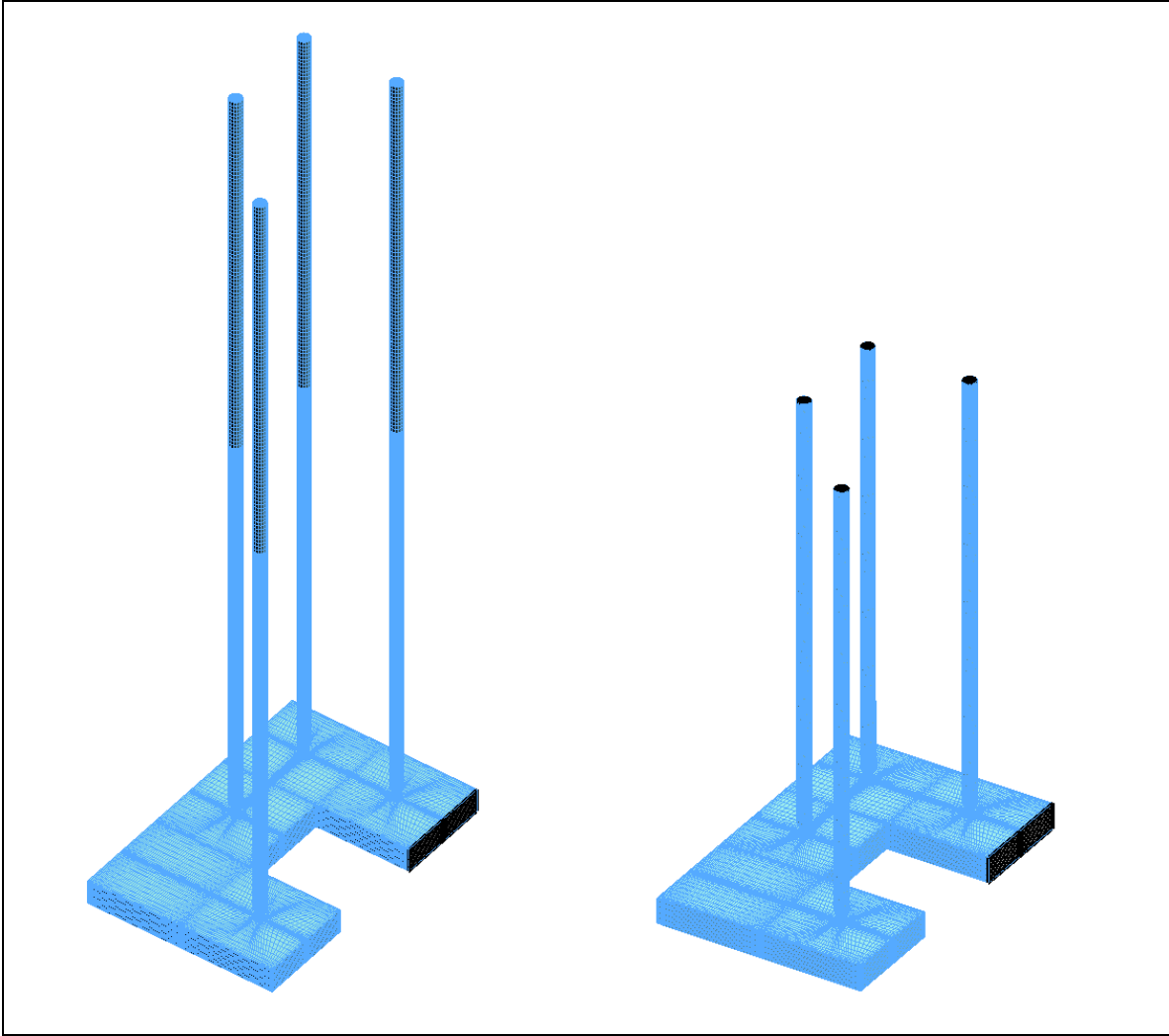


Figure 2.11: Two Different Channel Lengths used in Case 2

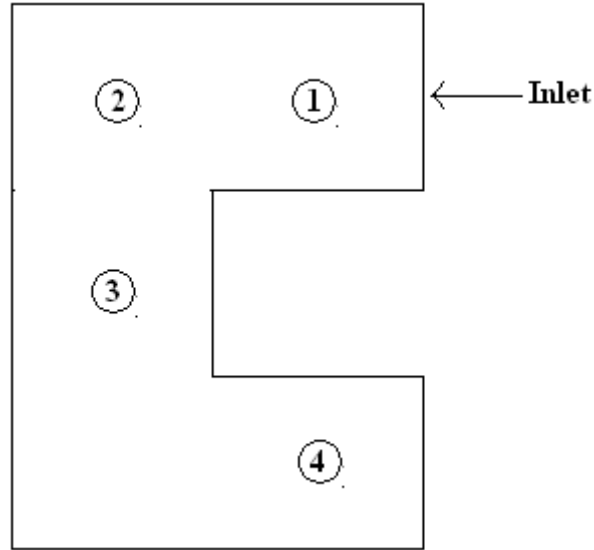


Figure 2.12: Top View/Schematic of Case 2

Table 2.4: Case 2 Results

Mass Flow Inlet into the Plenum (kg/s)		0.785	
Difference in Channel Length between the Models (mm)		400	
Channel	Mass Flow Rate (kg/s)		% difference (%)
	Original Length	Shorter Length	
1	0.2000	0.2000	0.04
2	0.2010	0.2009	0.04
3	0.1963	0.1959	0.23
4	0.1876	0.1882	-0.32

2.5 Calculation of Flow Distribution in the Heavy Reflector

Now that the method is validated, the focus goes back to the calculation of the flow distribution among the cooling channels in the heavy reflector. As discussed in section 2.1, the heavy reflector consists of Slab I at the bottom with a plenum and Slab II through XII with 832 cooling channels drilled through them. After simplifying, the computational model now includes only the plenum in Slab I and the cooling channels,

modeled up to the height of Slab II. The remaining length of the cooling channels, which is the total height of Slab III through XII, is represented by the outlet vent boundary condition set at the end of the channels at the top of Slab II. K_{eq} used for the outlet vent condition is again calculated using Equation (2.7) with K_o of 5.79 per orifice, or 57.9 for ten orifices per channel. The calculation of K_o is included in Appendix D. The model also includes the small holes on the side of the plenum, leading some of the flow into the gap between the heavy reflector and the core barrel. The amount of flow through these holes is fixed. In addition, the model is cut down to 1/8 using symmetry, cutting down the number of cooling channels included in the calculation to 104.

The resulting model has total of about 2.8 million cells, of which 1.8 million cells are in the cooling channels, and the rest is in the plenum. Each cooling channel has 208 cells per cross section with aspect ratio of 50 near the wall. The cooling channels are meshed so that the y-plus value near wall in these channels is between 40 and 60 for the calculated average flow rate. Each run takes about 10 hours using 2 CPUs, 2.66 GHz each, and about 3 GB of memory. The grid of the computational model is shown in Figure 2.13 through 2.16 in the next few pages. The tables following the figures show the settings in FLUENT used for the computation. The basic equations which are solved and the turbulence calculation are described in Appendices A and B. Refer to section 2.1 for the dimensions and explanations of the inlets. The turbulent length scale for any inlet or outlet is calculated by multiplying the corresponding hydraulic diameter by 0.07 as recommended in the FLUENT manual [8].

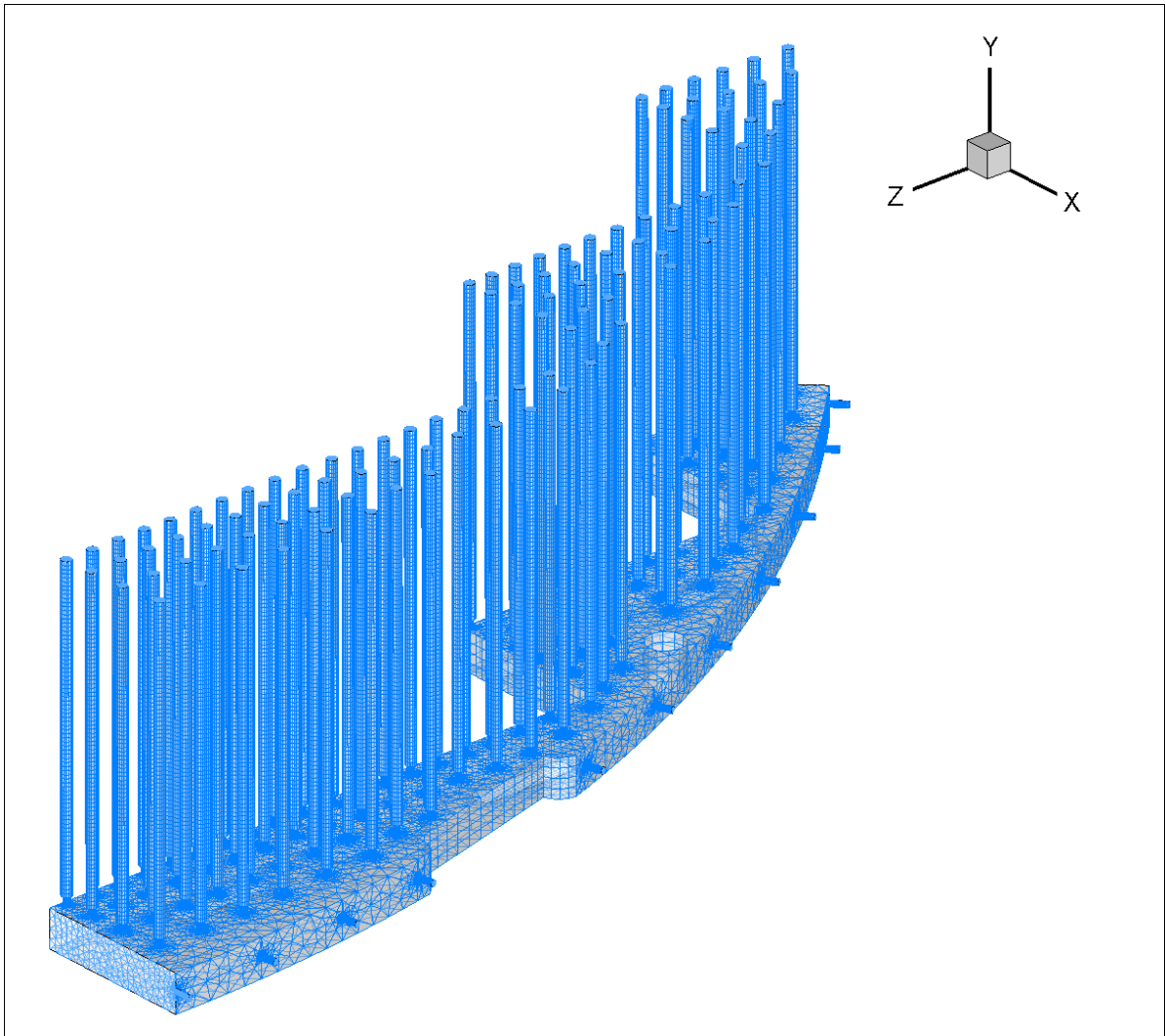


Figure 2.13: Computational Model for the Flow Distribution-Isometric View

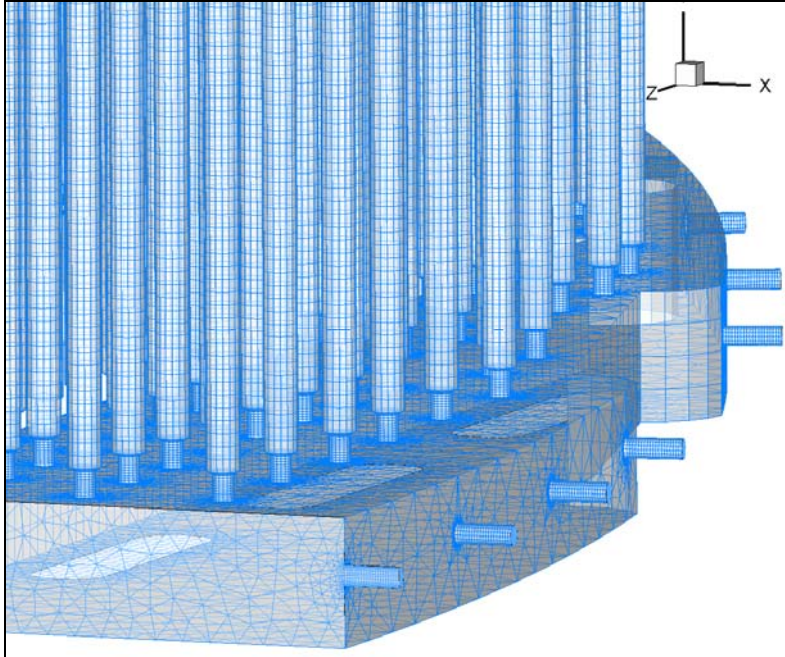


Figure 2.14: Close Up View of the Plenum in Slab I

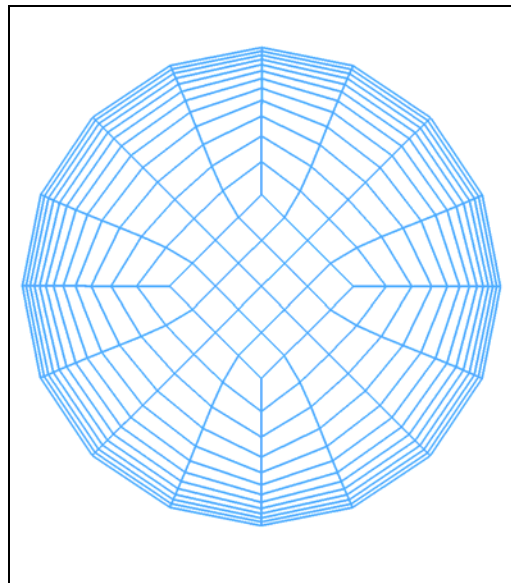


Figure 2.15: Mesh for the Cooling Channels-Top View

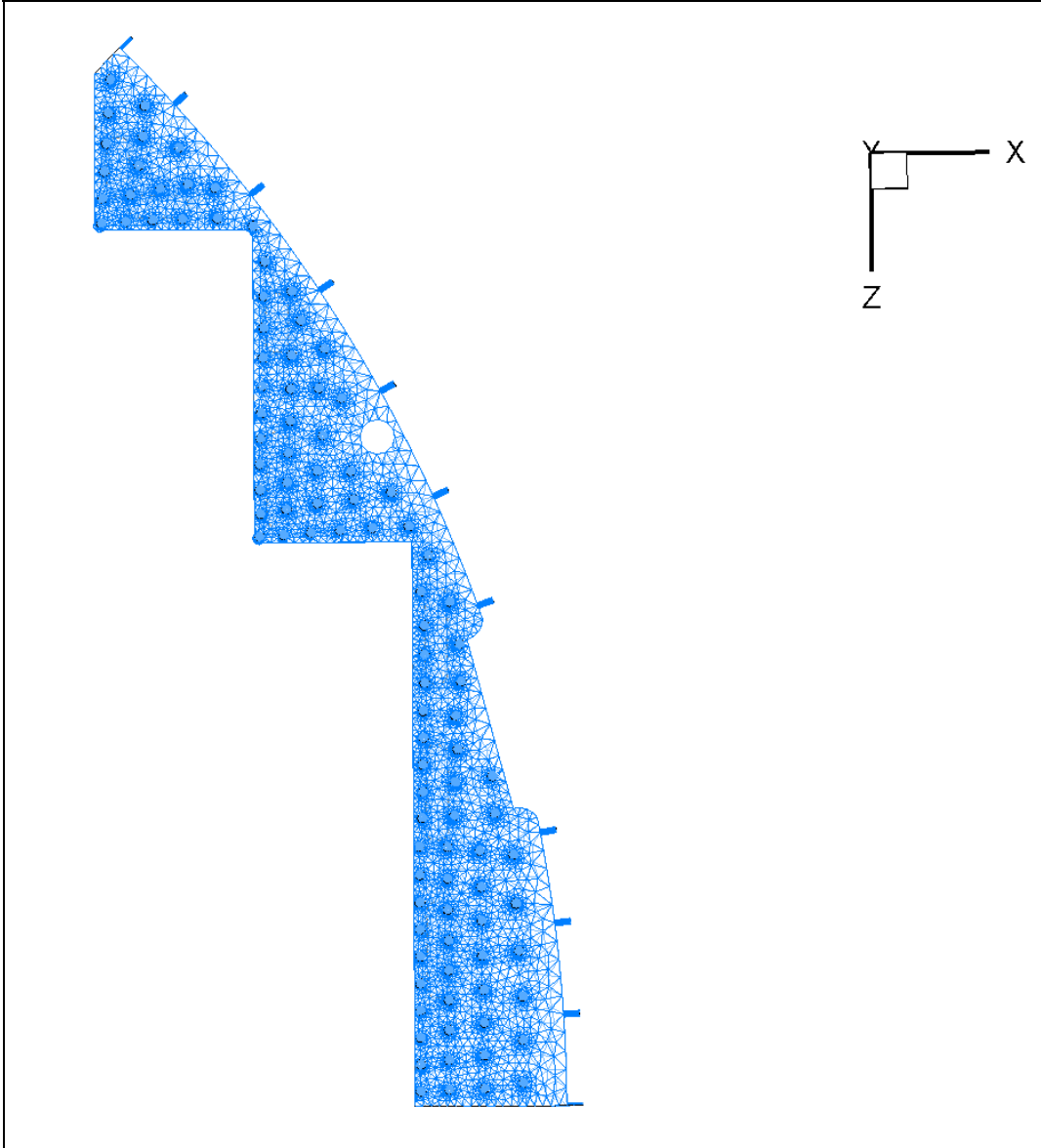


Figure 2.16: Computational Model for the Flow Distribution-Top View

Table 2.5: Solver Settings

Solver Type	Default
Viscous Model Type	RNG k-epsilon [2 eqn] Non-Equilibrium Wall Functions
Solution Control	Pressure-Velocity Coupling = SIMPLE Discretization: Pressure = Standard Momentum, Turbulent Kinetic Energy, And Turbulent Dissipation Rate = Second Order Upwind

Table 2.6: Inlet Conditions

Boundary Condition Type	Mass Flow Inlet
Mass Flow Rate-Large Inlets (kg/s)	4.408
Mass Flow Rate-Small Inlets (kg/s)	2.309
Turbulent Length Scale-Larger Inlet (m)	0.00917
Turbulent Length Scale-Smaller Inlet (m)	0.00567

Table 2.7: Outlet Conditions for Channel Outlets

Boundary Condition Type	Outlet Vent
K_{eq}	62.64
Turbulent Length Scale (m)	0.00091

Table 2.8: Flow to the Annulus

Boundary Condition Type	Mass Flow Inlet
Mass Flow Rate (kg/s)	0.417984*
Turbulent Length Scale (m)	0.000560

*Two of the outlets are only half size, thus the mass flow rates are also half.

*Direction is specified with vector so that the water flows out instead of in.

2.6 Results

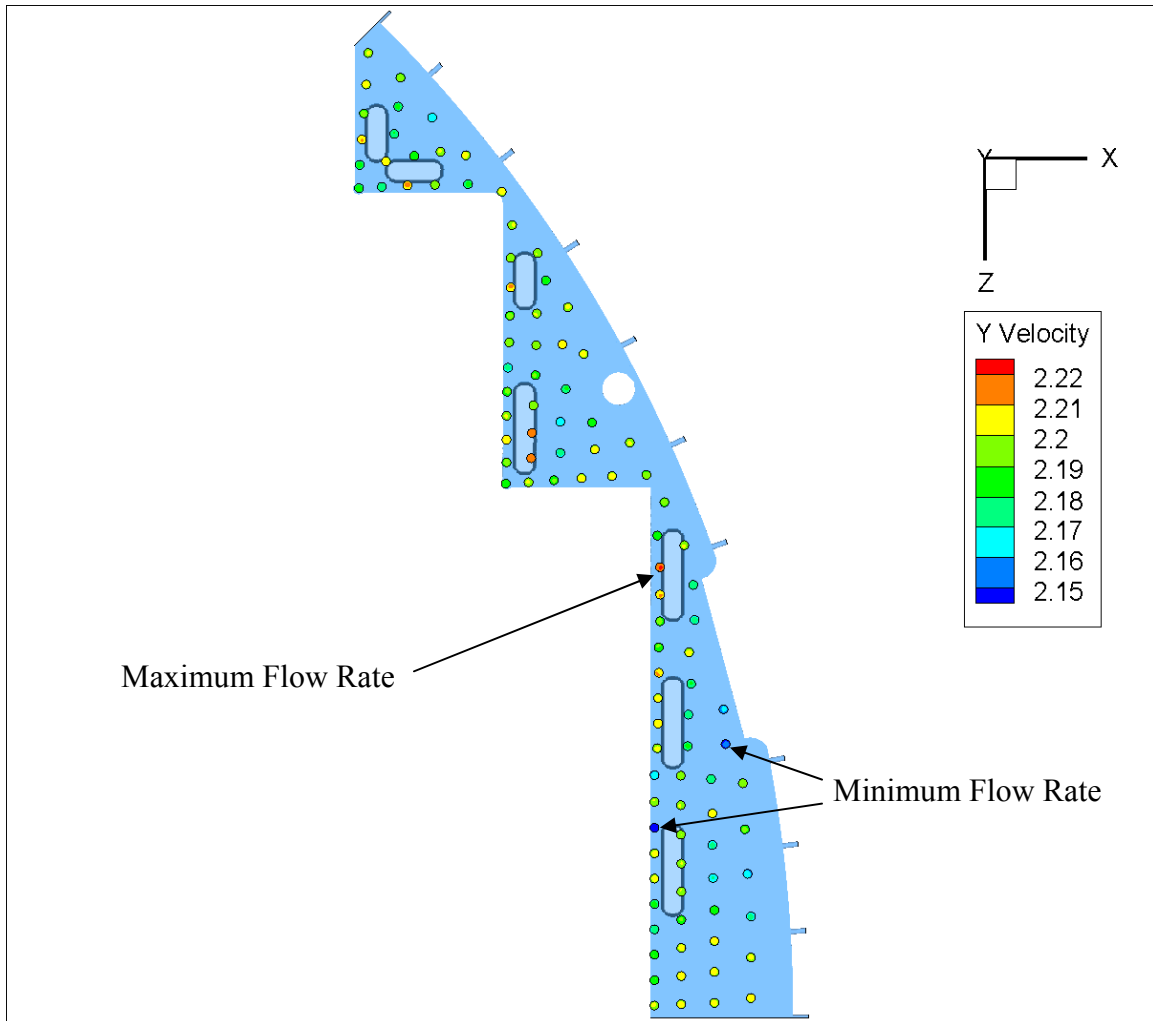


Figure 2.17: Flow Distribution with $K_{eq} = 62.6$

Table 2.9: Summary of the Flow Distribution with $K_{eq} = 62.6$

Average Flow Rate (kg/s)	0.196
Minimum Flow Rate (kg/s)	0.1917
Maximum Flow Rate (kg/s)	0.1983
% Difference Between Max and Min (%)	3.47

As shown in Figure 2.17, the flow rate is higher in the channels near the inlets, as expected. The highest flow rate is found in a channel above one of the larger inlets that is in a relatively small space. The lowest flow rates are found near the wall to the right of an inlet, which is the second one from the bottom, and near the inlet at the bottom. This is likely caused by the plenum suddenly opening up, letting more flow into the open space rather than the cooling channels. Overall, however, the difference in the flow rates between the channels is not large as shown in Table 2.9. The flow distribution is practically uniform.

A few more calculations are done using the same model to investigate the flow distribution even farther. In these calculations, the value of K_{eq} at the channel outlets is changed to 40 in one calculation and 0 in another. With $K_{eq} = 40$, the resulting flow distribution does not change much; the percent difference between the maximum and the minimum flow rates is 3.69 %. However, a more significant difference is found in the calculation with $K_{eq} = 0$. Figure 2.18 and Table 2.10 on the next page show the results of this calculation.

The channel locations where high and low flow rates are found are still very similar to that of the initial calculation with $K_{eq} = 62.6$. However, the percent difference between the maximum flow rate and the minimum flow rate becomes much higher when the value of K_{eq} at the outlets is lowered. From these calculation results, it is concluded that the uniform flow distribution in the initial calculation, with $K_{eq} = 62.6$, is caused by the significant difference between the flow resistance in the cooling channels, mostly due to the orifices, and that in the plenum. The orifices function properly as the flow calibration device, and there is practically no maldistribution of the flow among the cooling channels in the heavy reflector.

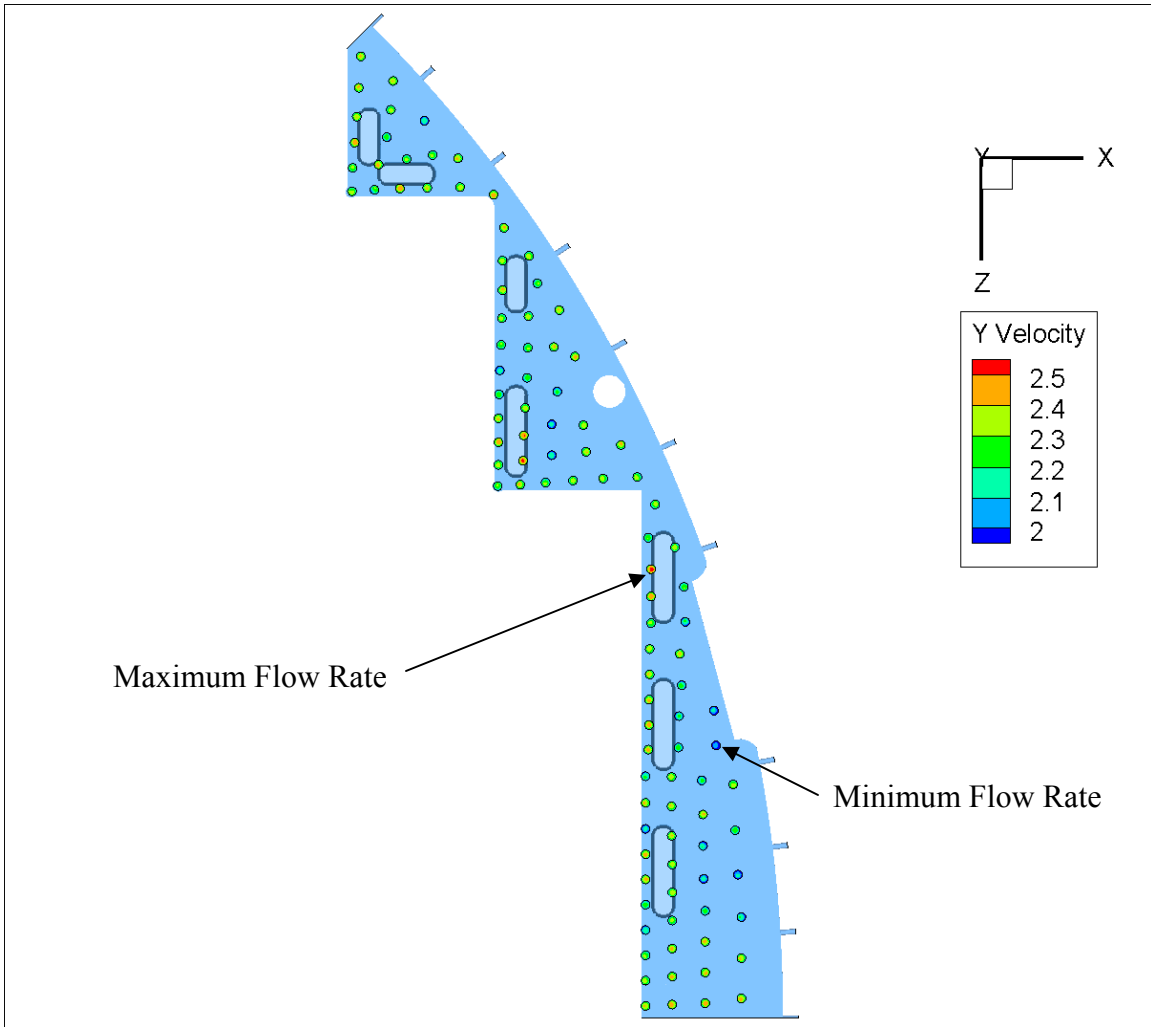


Figure 2.18: Flow Distribution with $K_{eq} = 0$

Table 2.10: Summary of Flow Distribution with $K_{eq} = 0$

Average Flow Rate (kg/s)	0.1960
Minimum Flow Rate (kg/s)	0.1726
Maximum Flow Rate (kg/s)	0.2125
% Difference Between Max and Min (%)	23.11

CHAPTER 3. TEMPERATURE DISTRIBUTION IN THE HEAVY REFLECTOR

In this chapter, the temperature distribution in the heavy reflector is calculated. The maximum temperature is to be determined to see if it exceeds the maximum allowable temperature of 350 °C. If the maximum temperature is higher than this value, this value has to be lowered by making some adjustments in the flow distribution among the cooling channels. The chapter proceeds in the following manner: description of the relevant geometry and the coolant flow paths, a list of material properties, grid sensitivity study on the flow fields associated with heat transfer, description of the grid used for the calculation, methodology for implementing the given heat source data in FLUENT, boundary conditions used in the computational model, and results.

3.1 Relevant Geometry and Coolant Flows

The general structure of the heavy reflector is described in section 2.1 in the previous chapter. The structure consists of twelve stainless steel slabs stacked together, axially restrained by vertical keys and tie rods. All the slabs except the one at the bottom are equipped with 832 cooling channels with 13 mm diameter drilled through them. Each channel has an 8 mm diameter orifice at the bottom of each slab. The slab at the bottom, Slab I, has a plenum that acts as the flow distribution plenum for the coolant. The coolant, which in this case is pressurized water, flows through the plenum and then through the cooling channels as well as other flow paths, including the gaps between the heavy reflector and various structures such as the core barrel, vertical keys, and tie rods. Tie rods also have some internal flow, which helps cool the heavy reflector in addition to the other coolant flows. The flow through the core also cools the heavy reflector. From previous studies, it is known that the heat transfer in Slab I is not significant; consequently, Slab I is not included in the heat transfer analysis. The other slabs, known as the typical slabs, are all identical except for the top slab which has a slightly larger diameter, 1460 mm instead of 1456 mm, and the slab below that has a 20 mm groove on

its outer diameter. The height of each slab is 417 mm. See Figures 2.1, 2.2, and 2.3 for more detail.

3.2 Material Properties

The only materials used in the calculation are water and stainless steel. Just like the flow distribution calculation in the previous chapter, the properties of water are assumed to be constant, due to the high operation pressure of the system. The water properties are taken at 315 °C, which is close to the average of the inlet and the outlet water temperatures of the reactor core. The properties of steel are also assumed to be constant and are taken from Reference [10]. These properties are shown in Tables 3.1 and 3.2. Minor components such as bolts in the reflector are neglected in the model for simplification purpose. They are small enough that they do not have any significant effect on the results.

Table 3.1: Water Properties

Density (kg/m ³)	691.9
Viscosity (kg/m-s)	0.00008241
Specific Heat (Cp) (J/kg-K)	5943
Thermal Conductivity (W/m-K)	0.5234

Table 3.2: Stainless Steel Properties

Density (kg/m ³)	7740
Specific Heat (Cp) (J/kg-K)	562.7
Thermal Conductivity (W/m-K)	19.563

3.3 Grid Sensitivity Study in the Coolant Flow Paths

The computational model for the conjugate heat transfer analysis has to include all of the coolant flows that extract heat from the heavy reflector slabs. As described in section 3.1, these flows include the ones through the core, the cooling channels, inside and around tie rods, the gap between the heavy reflector and the core barrel, and the gap between the heavy reflector and the vertical key. The free stream temperature profile is known for the flow through the core. By calculating the corresponding heat transfer coefficient, a convective boundary condition is used at the inner boundary of the reflector. The other coolant flow paths are included in the calculation. The expected Reynolds numbers for these flows, calculated based on the flow rates taken from the previous chapter as well as References [10] and [11], indicate that the all of the flows are turbulent. This causes problem with the computational cost for the calculation because turbulent flows require the mesh to be very fine for an accurate calculation of the flow field. The flow distribution calculation in the previous chapter does not have this problem since the model only includes Slabs I and II. However, for the heat transfer calculation, the model has to include eleven slabs, which in total is 4587 mm high. Modeling the coolant flow paths in high resolution for this much length would make the model computationally too expensive. In order to reduce the computational cost, a grid sensitivity study is conducted for each flow path to determine the minimum grid density that gives accurate results in heat transfer calculation.

Although each flow path is 4587 mm long, only one slab length, 417 mm, is analyzed in the study since that is enough to estimate the accuracy of the heat transfer calculation. Each flow path is initially modeled with a fine grid, and then the grid is made progressively coarser. The accuracy of the solution for the coarsened grid is determined by comparing the resulting average heat transfer coefficient with that of the initial, fine grid. For the purpose of the study, the solution of the coarsened grid is considered accurate if the difference in the average heat transfer coefficient for the initial grid and the coarsened grid is under 5%. The average heat transfer coefficient for the initial grid is

compared with the theoretical values calculated based on known correlations to make sure that its value is reasonable. The equations for the theoretical values are

$$\bar{h} = 0.023 \frac{k}{D_h} \text{Re}^{0.8} \text{Pr}^{0.4} \quad (3.1)$$

$$\bar{h} = 0.0214 \frac{k}{D_h} (\text{Re}^{0.8} - 100) \text{Pr}^{0.4} \quad (3.2)$$

$$\bar{h} = 0.0214 \frac{k}{D_h} (\text{Re}^{0.8} - 100) \text{Pr}^{0.4} \left(1 + \left(\frac{D_h}{L} \right)^{2/3} \right) \quad (3.3)$$

where \bar{h} is the average heat transfer coefficient, Re is the Reynolds number, Pr is the Prandtl number, D_h is the hydraulic diameter, k is the thermal conductance of the water, and L is the length in the flow direction. Equation (3.1) is based on Dittus-Boelter correlation for fully developed, turbulent flow and applies only to the fully developed region. Equations (3.2) and (3.3) are based on Gnielinski's correlation [9]. Equation (3.1) applies for the fully developed region, and Equation (3.3) applies to $0 < D_h/L < 1$, which includes the developing region. The average heat transfer coefficient for the fully developed region should be close to the values calculated with Equation (3.1) and (3.2), and that for the developing region should be close to the value calculated with Equation (3.3). All three correlations may have errors up to 20 %. Refer to Appendix E for more detail on these equations as well as the equation used to calculate the average heat transfer coefficients from CFD calculation results.

3.3.1 Cooling Channels

Based on the average Reynolds number in the cooling channels 230,000, found in section 2.3, the flow through the cooling channels is expected to take about 450 mm to become fully-developed. Since the channels have an orifice at the bottom of each slab, 417 mm apart from each other, the flows in the cooling channels never become fully-developed. However, the heat transfer coefficient is lower for a fully-developed region than that of the developing region; consequently, modeling the channels without the

orifices can simplify the computational model while making the heat transfer analysis more conservative. For this reason, the orifices are neglected in the computational model.

Without the orifices, the cooling channels are simply vertical channels with 13 mm diameter. For the purpose of the grid sensitivity study, the grid is varied in three different components: the distance between the wall and the first grid point from the wall Δy_1 , the cell height Δx , and the number of cells along the perimeter N . The water flows in the direction of Δx , and the distance from the inlet is denoted by x . An example of the grid is shown in Figure 3.1. The initial grid has values of $\Delta y_1 = 0.1$ mm, $\Delta x = 1$ mm, and $N = 32$. These values are then changed, one at a time, to see their effects on the heat transfer coefficient.

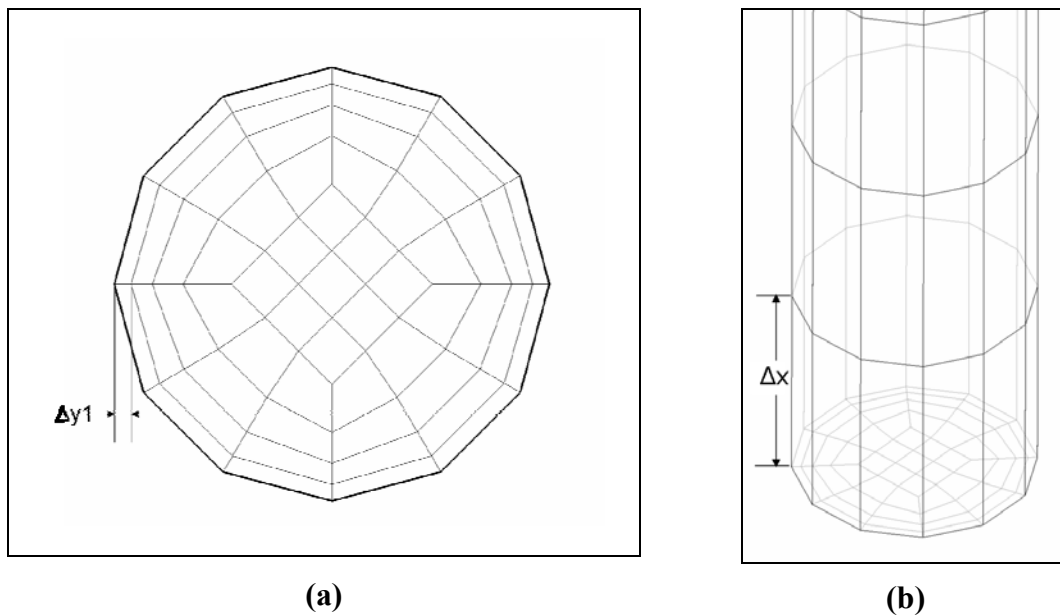


Figure 3.1: Variables (a) Δy_1 and (b) Δx in Cooling Channels

Table 3.3 shows the heat transfer coefficient calculated with the initial grid and the theoretical values. The value obtained from the initial grid is compared only with Equation (3.2) because the flow never becomes fully developed. The computational value and the theoretical value turn out to have 11.27 % difference, which is within the acceptable range of error; therefore, it is concluded that the initial grid gives accurate enough solution to be used as the reference grid for the study. The variation in each

variables, Δy_1 , Δx , and N and its effects are shown in Tables 3.4 through 3.6. From these results, it is determined that the best combination is $\Delta y_1 = 0.5$ mm, $\Delta x = 15$ mm, and $N = 12$, giving the least number of cells while keeping the integrity of the heat transfer calculation. This combination gives the total number of cells for 104 channels with eleven slabs 1,825,824 while the initial grid had 244,248,576 cells, and the resulting average heat transfer coefficient turns out to be 20196 W/m²-K, which is only 3.91 % different from that of the initial grid.

Table 3.3: Heat Transfer Coefficients for Cooling Channels ($\Delta y_1 = 0.1$ mm, $\Delta x = 1$ mm, and $N = 32$)

Theoretical Heat Transfer Coefficient (W/m ² -K)	
Gnielinski Developing (Equation (3.3))	18091
Average Heat Transfer Coefficient from CFD Model with the Initial Grid for $0 \text{ mm} < x < 400 \text{ mm}$	20130 (11.27 % difference from the theoretical value)

Table 3.4: Variation in Δy_1 and Resulting Heat Transfer Coefficients for Cooling Channels ($\Delta x/\Delta y_1 = 50$, $N = 16$)

Δy_1 (mm)	Total # of Cells for 104 Channels with 11 Slabs	\bar{h} (W/m ² -K) ($0 \text{ mm} < x < 400 \text{ mm}$)	% Difference from Initial Grid
0.2	6,150,144	20492	1.80
0.3	3,587,584	20248	0.59
0.4	2,306,304	21157	5.10
0.5	1,867,008	21249	5.56

Table 3.5: Variation in Δx and Resulting Heat Transfer Coefficients for Cooling Channels ($\Delta y_1 = 0.5$ mm, $N = 16$)

Δx (mm)	Total # of Cells for 104 Channels with 11 Slabs	\bar{h} (W/m ² -K) (0 mm < x < 400 mm)	% Difference from Initial Grid
15.00	3,075,072	20257	0.63
15.50	2,965,248	20220	0.45
16.00	2,855,424	20179	0.25
16.65	2,745,600	20136	0.03
17.50	2,635,776	21167	5.15
20.00	2,306,304	21175	5.19
25.00	1,867,008	21249	5.56

Table 3.6: Variation in N and the Resulting Heat Transfer Coefficients for Cooling Channels ($\Delta y_1 = 0.5$ mm, $\Delta x = 15$ mm)

N	Total # of Cells for 104 Channels with 11 Slabs	\bar{h} (W/m ² -K) (0 mm < x < 400 mm)	% Difference from Initial Grid
16	2,562,560	20336	1.02
12	1,825,824	20916	3.91
8	1,153,152	21938	8.98
4	544,544	29655	47.32

3.3.2 Gap Around Tie Rod

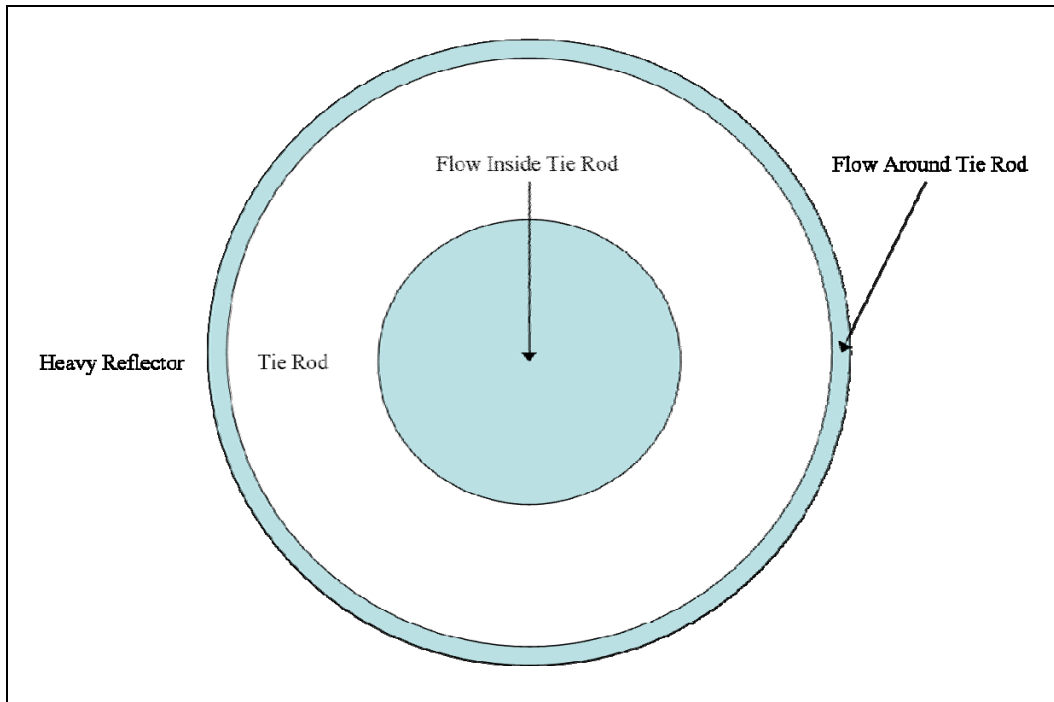


Figure 3.2: Top View of the Tie Rod and the Associated Flow Paths

There are two flow paths associated with tie rods, as shown in Figure 3.2. One is the flow inside the tie rod, and another is the gap between the tie rod and the heavy reflector. Just like the cooling channels, the grid for the gap around tie rods is varied in the same way with three variables, Δy_1 , Δx , and N . The number of cells in the radial direction is also adjusted depending on Δy_1 . The initial grid for this study has values of $\Delta y_1 = 0.2$ mm, $\Delta x = 1$ mm, and $N = 32$. Unlike the cooling channels, the flow becomes fully-developed before it reaches $x = 200$ mm. Therefore, the heat transfer coefficient in the fully-developed region is also recorded for additional validation. Table 3.7 shows the heat transfer coefficients from the theories and from the initial grid. The value of \bar{h} for 0 mm $< x < 400$ mm is 13.13 % different from that from Equation (3.3), and that for 200 mm $< x < 400$ mm where the flow is fully-developed is only 5.54 % off from Equation (3.1) and 15.28 % off from Equation (3.2). All of these values are within the acceptable range or error; therefore, the initial grid is legitimate as the reference grid for the study. The grid used for the study is shown in Figure 3.4, and the results of the study are shown

in Tables 3.8, 3.9, and 3.10 on the following pages. For labeling purpose, the region where $0 \text{ mm} < x < 400 \text{ mm}$ is called Region 1, and the region where $200 \text{ mm} < x < 400 \text{ mm}$ is called Region 2. These labeling apply to rest of the flow paths as well. From these results, the grid quality to be used for the heat transfer calculation is determined to be $\Delta y_1 = 0.75 \text{ mm}$, $\Delta x = 15 \text{ mm}$ (this value is chosen to agree with the cooling channel for meshing purpose), and $N = 16$ with 19,712 cells compared with the initial mesh with 1,321,056 cells. The difference in the average heat transfer coefficient for the initial grid and that for the final grid is only 1.93 % for region 1 and 0.77 % for region 2.

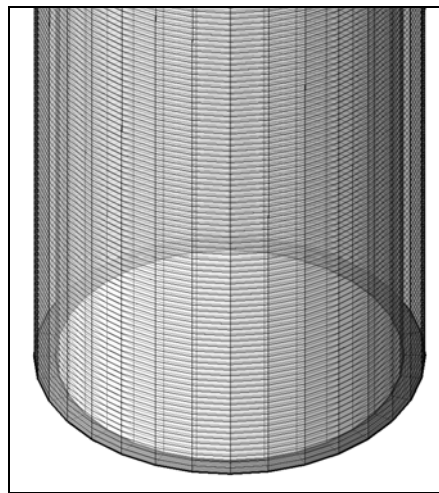


Figure 3.3: Isometric View of the Gap Around Tie Rod

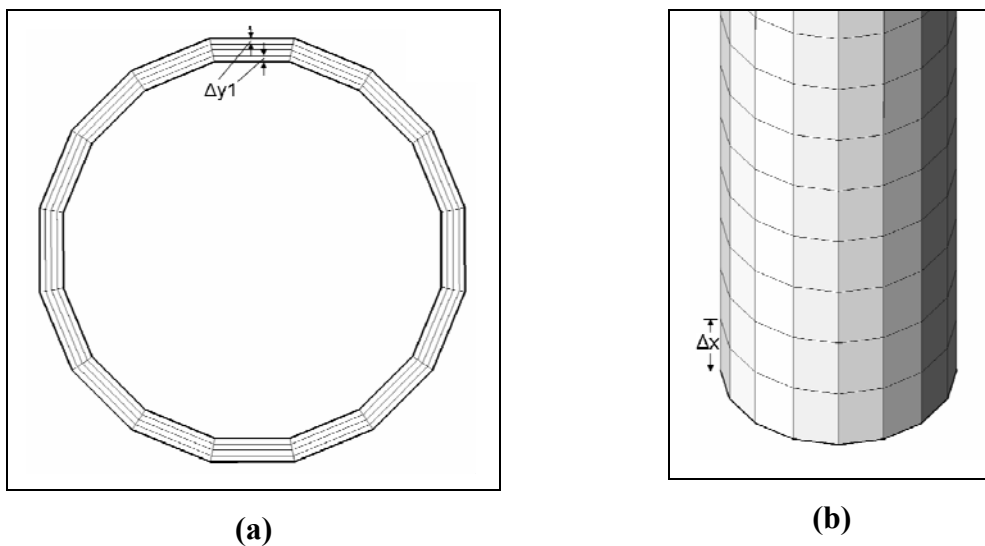


Figure 3.4: Variables (a) Δy_1 and (b) Δx for the Gap Around Tie Rod

Table 3.7: Heat Transfer Values in the Gap around the Tie Rod ($\Delta y_1 = 0.2$ mm, $\Delta x = 1$ mm, $N = 32$)

Theoretical Heat Transfer Coefficient (W/m^2-K)	
Dittus-Boelter (Equation (3.1))	12164
Gnielinski Fully-Developed (Equation (3.2))	11136
Gnielinski Developing (Equation (3.3))	11813
Average Heat Transfer Coefficient from CFD Model with the Initial Grid for Region 1 ($0 \text{ mm} < x < 400 \text{ mm}$)	13364 (13.13 % difference from Equation (3.3))
Average Heat Transfer Coefficient from CFD Model with Initial Grid for Region 2 ($200 \text{ mm} < x < 400 \text{ mm}$)	12838 (5.54 % difference from Equation (3.1) and 15.28 % difference from Equation (3.2))

Table 3.8: Variation in Δy_1 and Resulting Heat Transfer Coefficients with Percent Difference from the Initial Values for Gap around Tie Rod ($\Delta x = 1$ mm, $N = 32$)

Δy_1 (mm)	Total # of Cells for 11 Slabs	\bar{h} (W/m^2-K) (Region 1)	% Difference	\bar{h} (W/m^2-K) (Region 2)	% Difference
0.3	1,027,488	13425	0.45	12945	0.84
0.4	880,704	13514	1.12	13073	1.84
0.5	733,920	13416	0.39	12948	0.86
0.75	587,136	13410	0.34	12912	0.58
1.0	440,352	13593	1.71	13296	3.57
1.5	293,568	13612	1.85	13455	4.81

Table 3.9: Variation in Δx and Resulting Heat Transfer Coefficients with Percent Difference from the Initial Value for Gap around Tie Rod ($\Delta y_1 = 0.2$ mm, $N = 32$)

Δx (mm)	Total # of Cells for 11 Slabs	\bar{h} (W/m ² -K) (Region 1)	% Difference	\bar{h} (W/m ² -K) (Region 2)	% Difference
2	658,944	13379	0.11	12867	0.23
4	329,472	13347	-0.13	12865	0.22
8	164,736	13286	0.58	12879	0.21
16	82,368	13101	-1.96	12264	-4.47

Table 3.10: Variation in N and Resulting Heat Transfer Coefficients with Percent Difference from the Initial Value for Gap around Tie Rod ($\Delta y_1 = 0.2$ mm, $\Delta x = 1$ mm)

N	Total # of Cells for 11 Slabs	\bar{h} (W/m ² -K) (Region 1)	% Difference	\bar{h} (W/m ² -K) (Region 2)	% Difference
16	660,528	13585	1.65	13083	1.91
12	495,396	13819	3.40	13324	3.79
8	330,264	14621	9.40	14084	9.71

3.3.3 Flow Inside the Tie Rod

The flow inside the tie rod is practically the same geometry as the cooling channels, except the diameter is 20 mm instead of 13 mm with no orifices. The studied grid variables are the same as those for the cooling channels; however, only Δy_1 is varied in this case because both Δx and N are dependent on the grid for the gap around the tie rod, which is already determined. Only the initial grid has different values of Δx and N just to make sure of its accuracy. The initial grid has the values of $\Delta y_1 = 0.2$ mm, $\Delta x = 1$ mm, and $N = 32$. The resulting heat transfer coefficients are shown in Table 3.11. Again, the values obtained from the CFD model with the initial grid are fairly close to the theoretical values. The variation in Δy_1 and the resulting coefficients are listed in Table

3.12. From the results, it is determined that having $\Delta y_1 = 1.0$ mm does not give too large of an error. Since the number of cells in this region is not as large as the other regions, there is no need to coarsen the grid more; consequently, the combination of $\Delta y_1 = 1.0$ mm, $\Delta x = 15$ mm, and $N = 16$ is used in the overall calculation. This gives a total of 19,712 cells while the initial mesh has 2,642,112 cells, and the average heat transfer coefficient that is only 3.57 % different from the initial value.

Table 3.11: Heat Transfer Coefficient Values in the Flow Inside Tie Rod ($\Delta y_1 = 0.2$ mm, $\Delta x = 1$ mm, $N = 32$)

Theoretical Heat Transfer Coefficient (W/m ² -K)	
Dittus-Boelter (Equation (3.1))	6854
Gnielinski Fully-Developed (Equation (3.2))	6322
Gnielinski Developing (Equation (3.3))	7180
Average Heat Transfer Coefficient from CFD Model with the Initial Grid for Region 1 (0 mm < x < 400 mm)	8208 (14.31 % difference from Equation (3.3))
Average Heat Transfer Coefficient from CFD Model with the Initial Grid for Region 2 (200 mm < x < 400 mm)	7088 (3.42 % difference from Equation (3.1) and 12.12 % difference from Equation (3.2))

Table 3.12: Variation in Δy_1 and Resulting Heat Transfer Coefficients with Percent Difference from the Initial Value for Flow Inside Tie Rod ($\Delta x = 15$ mm, $N = 16$)

Δy_1 (mm)	Total # of Cells for 11 Slabs	\bar{h} (W/m ² -K) (Region 1)	% Difference	\bar{h} (W/m ² -K) (Region 2)	% Difference
0.3	44,352	13425	0.45	12945	0.84
0.4	39,424	13514	1.12	13073	1.84
0.5	34,496	13416	0.39	12948	0.86
0.75	24,640	13410	0.34	12912	0.58
1.0	19,712	13593	1.71	13296	3.57

3.3.4 Gap between the Heavy Reflector and the Core Barrel

For the purpose of study, the flow through the gap between the heavy reflector and the core barrel is modeled as a flow between two flat plates with symmetry boundary conditions set on each side since the radius of this gap region is much larger than the thickness of the gap. Just like the other flow paths, its grid is varied in three different components, but with the cell width along the wall, Δy_2 , instead of N . The initial grid for this study has $\Delta y_1 = 0.2$ mm, $\Delta y_2 = 1$ mm, and $\Delta x = 1$ mm. The resulting heat transfer coefficient for this grid and the theoretical values are shown in Table 3.13. Again, the theoretical values and the computed values match reasonably well. The variation in each component and its results are shown in Tables 3.14, 3.15, and 3.16. With these results, the cell quality to be used in the heat transfer analysis is determined to be $\Delta y_1 = 0.5$ mm, $\Delta y_2 = 25$ mm, and $\Delta x = 15$ mm. Δx is determined based on the other flow paths. This gives the total number of cells 42,381 compared with 36,818,790 for the initial mesh, and the average heat transfer coefficient that is 0.72 % different from the initial value.

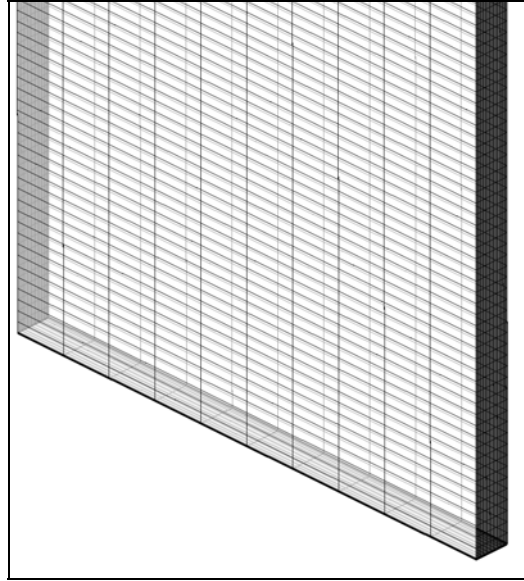
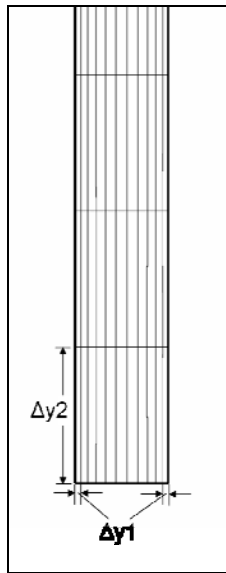
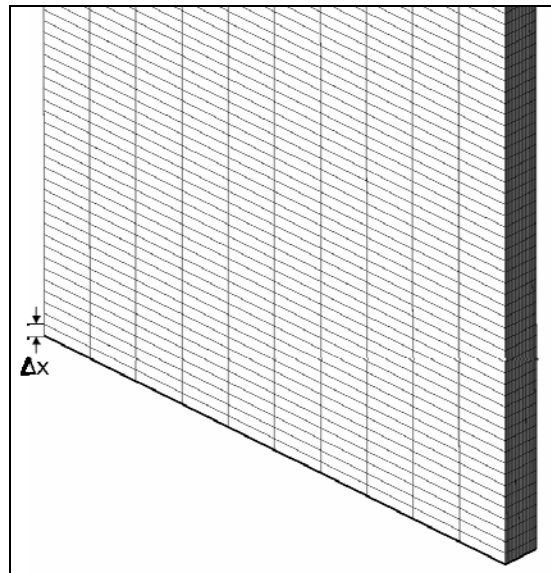


Figure 3.5: Overview of the Gap between the Heavy Reflector and the Core Barrel



(a)



(b)

Figure 3.6: Variables (1) Δy_1 , Δy_2 , and (2) Δx for Gap between the Heavy Reflector and the Core Barrel

Table 3.13: Reference Heat Transfer Values for Gap between the Heavy Reflector and the Core Barrel ($\Delta y_1 = 0.2$ mm, $\Delta y_2 = 1$ mm, $\Delta x = 1$ mm)

Theoretical Heat Transfer Coefficient (W/m ² -K)	
Dittus-Boelter (Equation (3.1))	11773
Gnielinski Fully-Developed (Equation (3.2))	10794
Gnielinski Developing (Equation (3.3))	11508
Average Heat Transfer Coefficient from CFD Model with the Initial Grid for Region 1 (0 mm < x < 400 mm)	12353 (7.34 % difference from Equation (3.3))
Average Heat Transfer Coefficient from CFD Model with the Initial Grid for Region 2 (200 mm < x < 400 mm)	11763 (0.09 % difference from Equation (3.1) and 8.98 % difference from Equation (3.2))

Table 3.14: Variation in Δy_1 and Resulting Heat Transfer Coefficients with Percent Difference from Initial Value for the Gap between the heavy Reflector and the Core Barrel ($\Delta y_2 = 1$ mm, $\Delta x = 1$ mm)

Δy_1 (mm)	Total # of Cells for 11 Slabs	\bar{h} (W/m ² -K) (Region 1)	% Difference	\bar{h} (W/m ² -K) (Region 2)	% Difference
0.3	23,669,222	12437	0.68	11886	0.95
0.4	18,409,395	12503	1.21	12001	1.93
0.5	15,779,481	12630	2.24	12197	3.60

Table 3.15: Variation in Δy_2 and Resulting Heat Transfer Coefficients with Percent Difference from Initial Value for the Gap between the heavy Reflector and the Core Barrel ($\Delta y_1 = 0.2$ mm, $\Delta x = 1$ mm)

Δy_2 (mm)	Total # of Cells for 11 Slabs	\bar{h} (W/m ² -K) (Region 1)	% Difference	\bar{h} (W/m ² -K) (Region 2)	% Difference
2	14,464,525	12351	-0.01	11762	-0.10
5	5,785,810	12350	-0.02	11761	-0.11
10	2,892,905	12343	-0.08	11754	-0.16
25	1,157,162	12349	-0.03	11760	-0.11

Table 3.16: Variation in Δx and Resulting Heat Transfer Coefficients with Percent Difference from Initial Value for the Gap between the heavy Reflector and the Core Barrel ($\Delta y_1 = 0.2$ mm, $\Delta y_2 = 1$ mm)

Δx (mm)	Total # of Cells for 11 Slabs	\bar{h} (W/m ² -K) (Region 1)	% Difference	\bar{h} (W/m ² -K) (Region 2)	% Difference
2	14,429,837	12367	0.11	11791	0.15
4	7,214,919	12337	-0.13	11790	0.14
8	3,607,459	12283	0.57	11798	0.20
16	1,803,730	12107	-1.99	11223	-4.68

3.3.5 Gap between the Heavy Reflector and the Vertical Key

The model used for studying the flow through the gap between the heavy reflector and the vertical key is similar to that from the previous section. Only differences are the dimensions and that the symmetry boundaries are replaced with simple walls. From previous section, it is notable that the change in Δx does not make much difference, so the variation in Δx is neglected in this study. The results are shown in Tables 3.17, 3.18 and 3.19 on the following pages. Note that the variation in Δy_1 in Table 3.18 seems to give a more random effect on the heat transfer coefficient when Δy_1 is more than 0.5 mm, although the error is not large. From this result, it is suspected that the solution may be unreliable in the range of $\Delta y_1 \geq 0.5$ mm because the grid is too coarse. Consequently, $\Delta y_1 = 0.4$ mm is chosen. The resulting combination is $\Delta y_1 = 0.4$ mm, $\Delta y_2 = 1.6$ mm, and $\Delta x = 15$ mm, which has a total of 29,260 cells while the original has 1,403,622 cells. The average heat transfer coefficient for this grid is 1.75 % off the initial value. The value of Δy_2 could have been 3 rather than 1.6; however, the number of cells is small enough in this region, so it is not of importance. This concludes the grid sensitivity study of the fluid region in the heat transfer analysis model.

Table 3.17: Reference Heat Transfer Values for the Gap between the Heavy Reflector and the Vertical Key ($\Delta y_1 = 0.2$ mm, $\Delta y_2 = 0.2$ mm, $\Delta x = 1$ mm)

Theoretical Heat Transfer Coefficient (W/m^2-K)	
Dittus-Boelter (Equation (3.1))	16129
Gnielinski Fully-Developed (Equation (3.2))	14725
Gnielinski Developing (Equation (3.3))	15394
Average Heat Transfer Coefficient from CFD Model with the Initial Grid for Region 1 ($0 \text{ mm} < x < 400 \text{ mm}$)	17249 (12.05 % difference from Equation (3.3))
Average Heat Transfer Coefficient from CFD Model with the Initial Grid for Region 2 ($200 \text{ mm} < x < 400 \text{ mm}$)	16756 (3.89 % difference from Equation (3.1) and 13.79 % difference from Equation (3.2))

Table 3.18: Variation in Δy_1 and Resulting Heat Transfer Coefficients with Percent Difference from Initial Value for the Gap between the heavy Reflector and the Vertical Key ($\Delta y_2 = 0.2$ mm, $\Delta x = 15$ mm)

Δy_1 (mm)	Total # of Cells for 11 Slabs	\bar{h} (W/m^2-K) (Region 1)	% Difference	\bar{h} (W/m^2-K) (Region 2)	% Difference
0.3	62,832	17232	-0.10	16418	1.79
0.4	52,360	17200	-0.29	16366	1.47
0.5	41,888	16766	-2.80	15695	-2.69
0.6	31,416	16886	-2.11	15904	-1.40
1	20,944	17362	0.65	16573	2.75

Table 3.19: Variation in Δy_2 and Resulting Heat Transfer Coefficients with Percent Difference from Initial Value for the Gap between the heavy Reflector and the Vertical Key ($\Delta y_1 = 0.2$ mm, $\Delta x = 15$ mm)

Δy_2 (mm)	Total # of Cells for 11 Slabs	\bar{h} (W/m ² -K) (Region 1)	% Difference	\bar{h} (W/m ² -K) (Region 2)	% Difference
0.4	80,388	16985	-1.53	16101	-0.17
0.8	66,528	16926	-1.87	16070	-0.37
1.6	52,668	16779	-2.73	15945	-1.14
3	38,808	16383	-5.02	15512	-3.83
6	24,948	15377	-10.85	14306	-11.30

3.4 Grid for the Heat Transfer Analysis

The heat conduction in the solid region can be accommodated on a reasonable mesh density and hence no independent grid sensitivity study is conducted for this region. The grid for the solid region refined once, and a part of the grid before and after the refinement is shown in Figure 3.7. Using the grid for the fluid region, determined in section 3.3, the grid for both the solid and the fluid regions is extruded vertically with each step being 15 mm apart. The complete model is shown in Figure 3.8 and 3.9. Figure 3.8 does not show the fluid region. The horizontal lines in Figure 3.9 are the lines separating the slabs. The total number of cells for the model, including both the fluid and the solid region, is about 9 million cells. Note that only 1/8 of the entire heavy reflector is modeled because of the symmetry in the geometry, just like the model in the previous chapter. Using 6 CPUs (2.66 GHz each) with standard k- ϵ turbulence model, standard wall functions, and second-order upwind discretization on all parameters, the computation of the momentum equation for this model takes about three hours. Memory usage for the calculation is around 10 GBs. The computation for the energy equation takes a very short time once the momentum equations are solved.

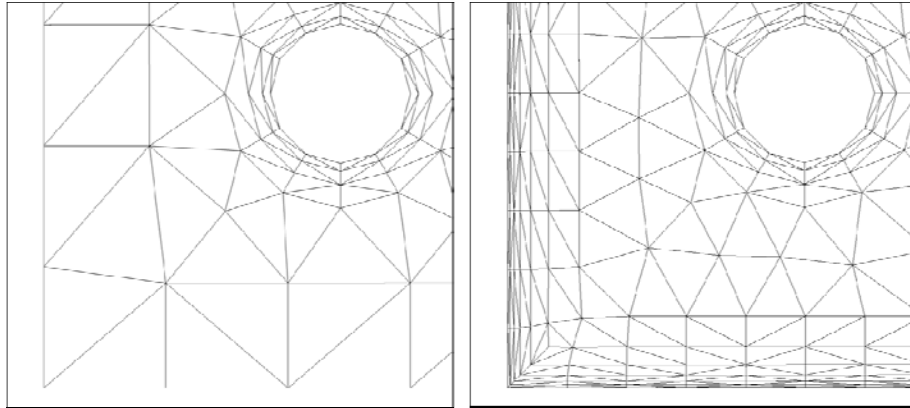


Figure 3.7: Refinement of the Solid Region

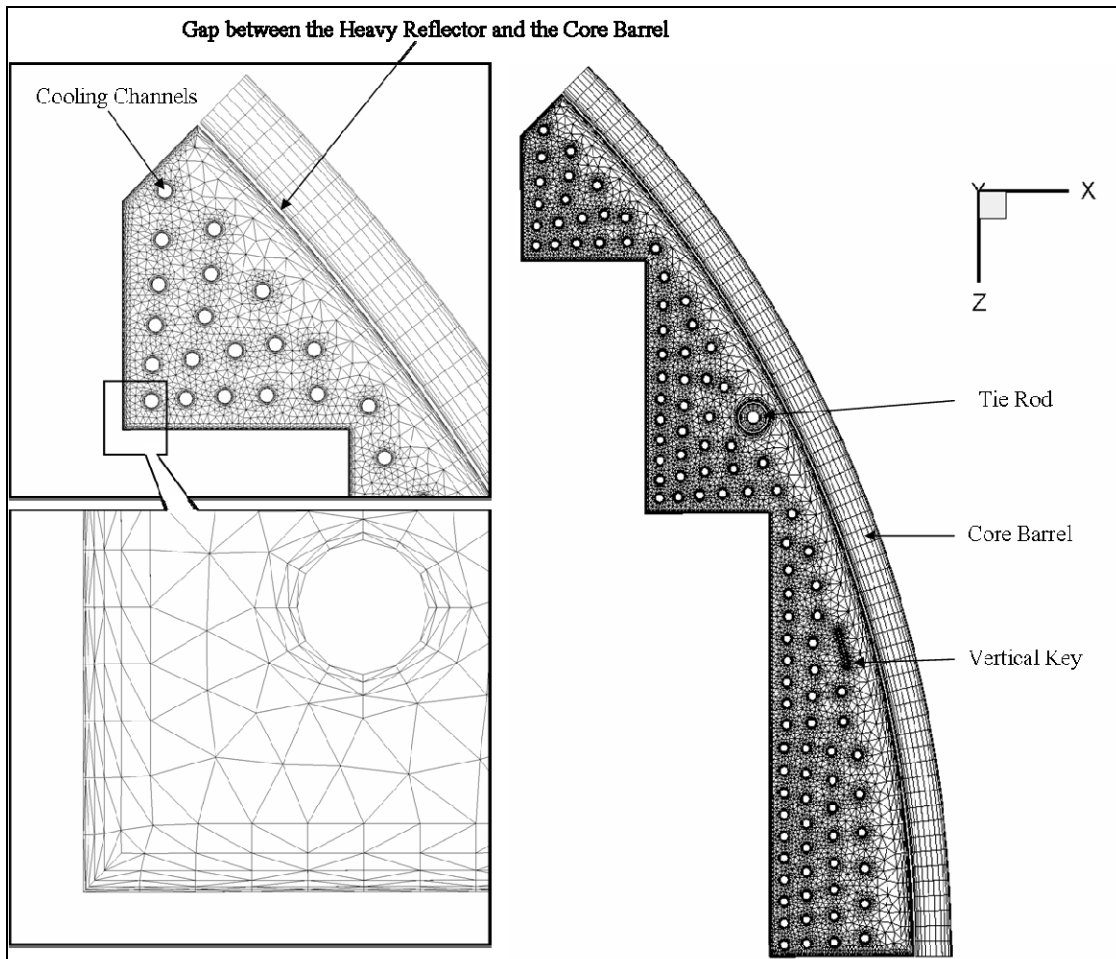


Figure 3.8: Top View of the Heat Transfer Model

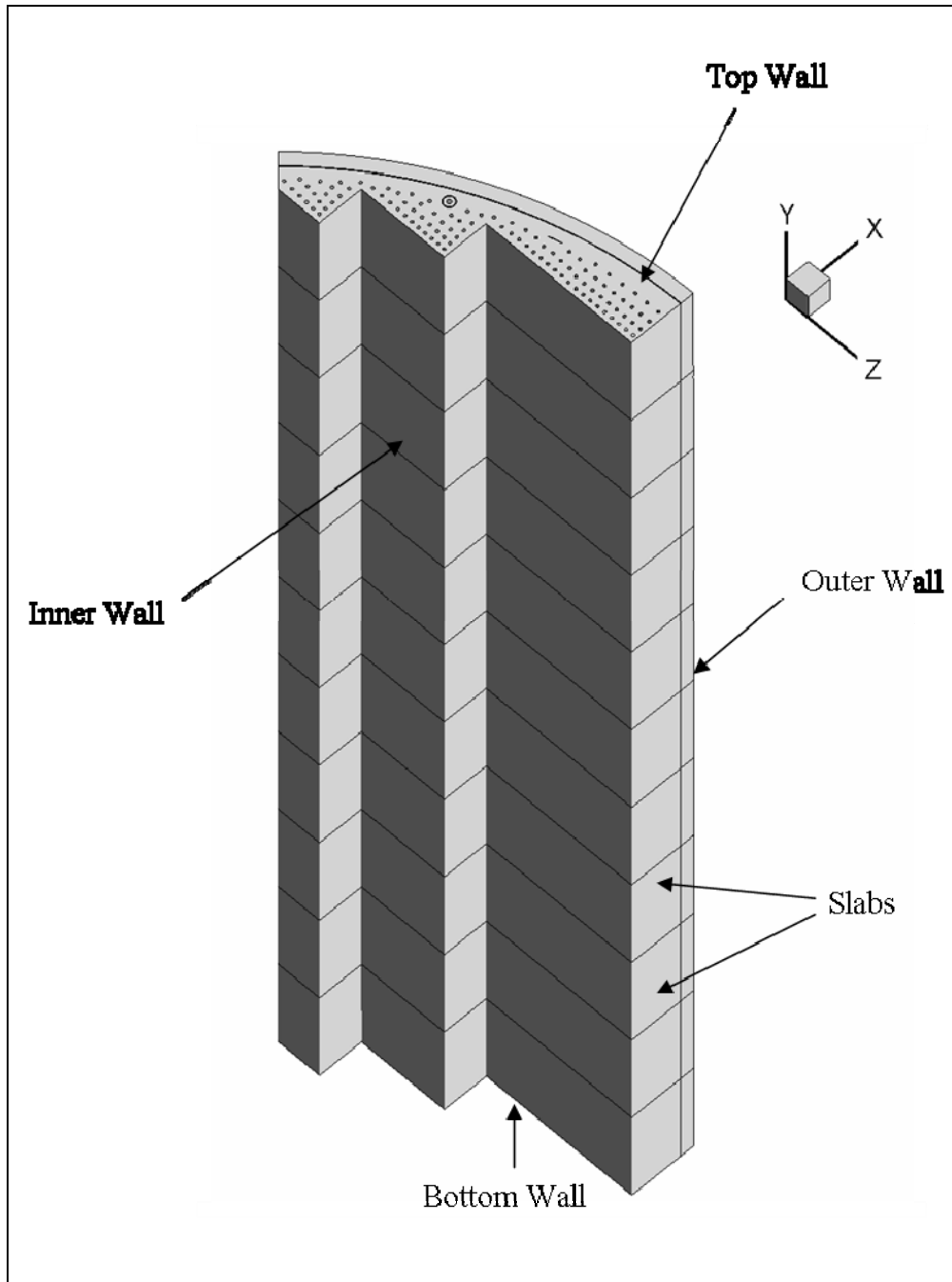


Figure 3.9: Isometric View of the Heat Transfer Model

3.5 Implementation of Heat Source Data in FLUENT

The main source of heat for the heavy reflector is the gamma radiation. Some of the gamma rays are emitted from the core during the fission process, while some more are emitted during the reaction between the heavy reflector material and the neutron flux, which also comes from the core. The heavy reflector is heated due to absorption of these gamma rays. The water flowing through the core may also heat up the reflector if the water happens to be hotter than the reflector at certain location; however, this is a very minor source compared to the heating due to absorption of gamma radiation. The temperature of the water flowing through the core is given in page 28 of Reference [2]. The heat generation in the solid region due to absorption of gamma radiation is calculated and given in Reference [11]. The shape of the heat generation distribution in the radial and the azimuthal directions is the same at any given height; however, the magnitude is different for each height. Therefore, the data is given in two different components, a two-dimensional data that contains the variation of the heat generation in the radial and the azimuthal directions, and a set of curve fit equations that define the axial profile. The axial profile is given in terms of a factor which is a function of height. The two dimensional data is for the height where the factor is equal to 1. The magnitude of the heat generation at each height is then given by multiplying this two dimensional data by the factor calculated using the curve fit equations. Note that Reference [11] shows several different axial profiles; however, for the purpose of this analysis, only the one for steady state calculation, which is labeled as “best-estimate axial profile” in Reference [11], is used. In addition, Reference [11] assumes that there is no heat generation in the fluid region; therefore, the same assumption is used for the heat transfer analysis as well.

In order to use this data in FLUENT, a MATLAB code is written to take the two-dimensional data, multiply it by the factor at each incremented height, and export a three-dimensional data table in a format appropriate to FLUENT. Both the MATLAB code and the data format are given in Appendices F and G. This three-dimensional data is then interpolated using the interpolation feature in FLUENT. However, this feature is intended

to read profile data, such as velocity profiles; therefore, the three-dimensional data cannot be read as a heat source as it is. In order to interpolate the data, features called a user-defined scalar (UDS) and user-defined memory (UDM) are used.

A UDS is a feature provided by FLUENT for the user to include additional data to be calculated. A UDM is another feature that can store data. The difference between a UDS and a UDM is that a UDS is a variable to be calculated, such as velocity or temperature, while a UDM is a set of constant values. The interpolation feature in FLUENT only accepts variable data; therefore the interpolated heat source data can only be stored as a UDS. On the other hand, the heat source setting in the solid region only accepts constants; consequently the data has to be converted in to a UDM. The conversion between these two data types is done using a user-defined function (UDF), which is a code written by the user. The purpose of UDF is to let the user use features that are not originally included in FLUENT. The UDF file used for the conversion is taken from ANSYS Online Technical Support and is included in Appendix H.

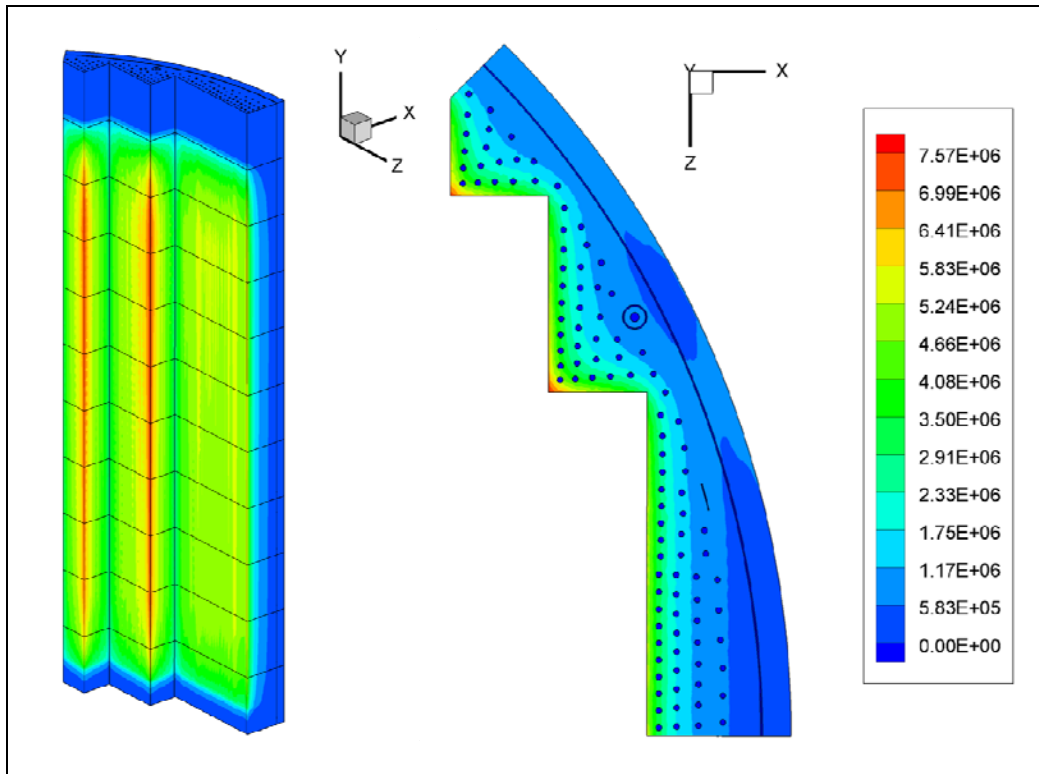


Figure 3.10: Heat Generation due to Gamma Radiation (W/m^3)

A three dimensional contour of the heat source data used in FLUENT is shown in the Figure 3.10. In order to make sure that this data is implemented correctly, a comparison is made between the total heat generation calculated within FLUENT using its volume integral feature and that calculated by hand. The calculation by hand is done by taking an average heat generation per cubic meter from the data table and multiplying by the volume. This is a rough estimate since the distribution of the given data points used for the data table is not exactly uniform; however, it is good enough for a quick check. The value found by the hand calculation is 1,987,026 W, and the value calculated in FLUENT is 2,015,483 W. These values are only 1.43 % apart from each other; therefore, it is concluded that the data is implemented appropriately.

3.6 Boundary Conditions

The flow rate of the water in the cooling channels is taken from Chapter 2. The rest of the flow rates used are taken from Reference [2] and [10]. Turbulence condition is set with turbulence intensity and length scale mode, where turbulence length scale is set as 0.07 times the hydraulic diameter as recommended in the FLUENT User's Manual [8]. The inlet boundary conditions for the coolant flow paths are shown in Tables 3.20 through 3.22. The outlet is set as a pressure outlet with default values for all flow paths. Since the flow rate in each path is known, the exact value of the pressure is not of importance. Turbulence length scale for each outlet is set as the same as that for the corresponding inlet.

The walls involved in the calculation are shown in Figure 3.9 in section 3.4. These include the inner wall of the heavy reflector facing the core, the outer wall of the core barrel facing the space outside the core, the bottom wall where Slab II is facing the flow distribution chamber in Slab I, and the top wall which is at the outlet on Slab XII. The boundary conditions for all the walls except the inner wall are taken from Reference [2] and [10].

Table 3.20: Mass Flow Inlets

Flow Path	Mass Flow Rate (kg/s)	Turbulence Length Scale (m)
Cooling Channels	0.196	0.00091
Around Tie Rod	0.3651	0.00042
Through Tie Rod	0.1574	0.0014

Table 3.21: Velocity Inlets

Flow Path	Flow Rate (m/s)	Turbulence Length Scale (m)
HR/CB Gap	1.0875	0.000271
HR/VK Gap	1.4	0.000476

Table 3.22: Inlet Temperature

Inlet Temperature for All Paths	568.15 K
---------------------------------	----------

Table 3.23: Wall Boundary Conditions

Wall	Ambient Temperature (K)	Heat Transfer Coefficient (W/m ² -K)
Inner Wall	Profile shown in Figure 3.11 with Curve Fit Equations shown in Figure 3.12	35000
Outer Wall	568.15	23200
Bottom Wall	568.15	5000
Top Wall	Adiabatic Wall	

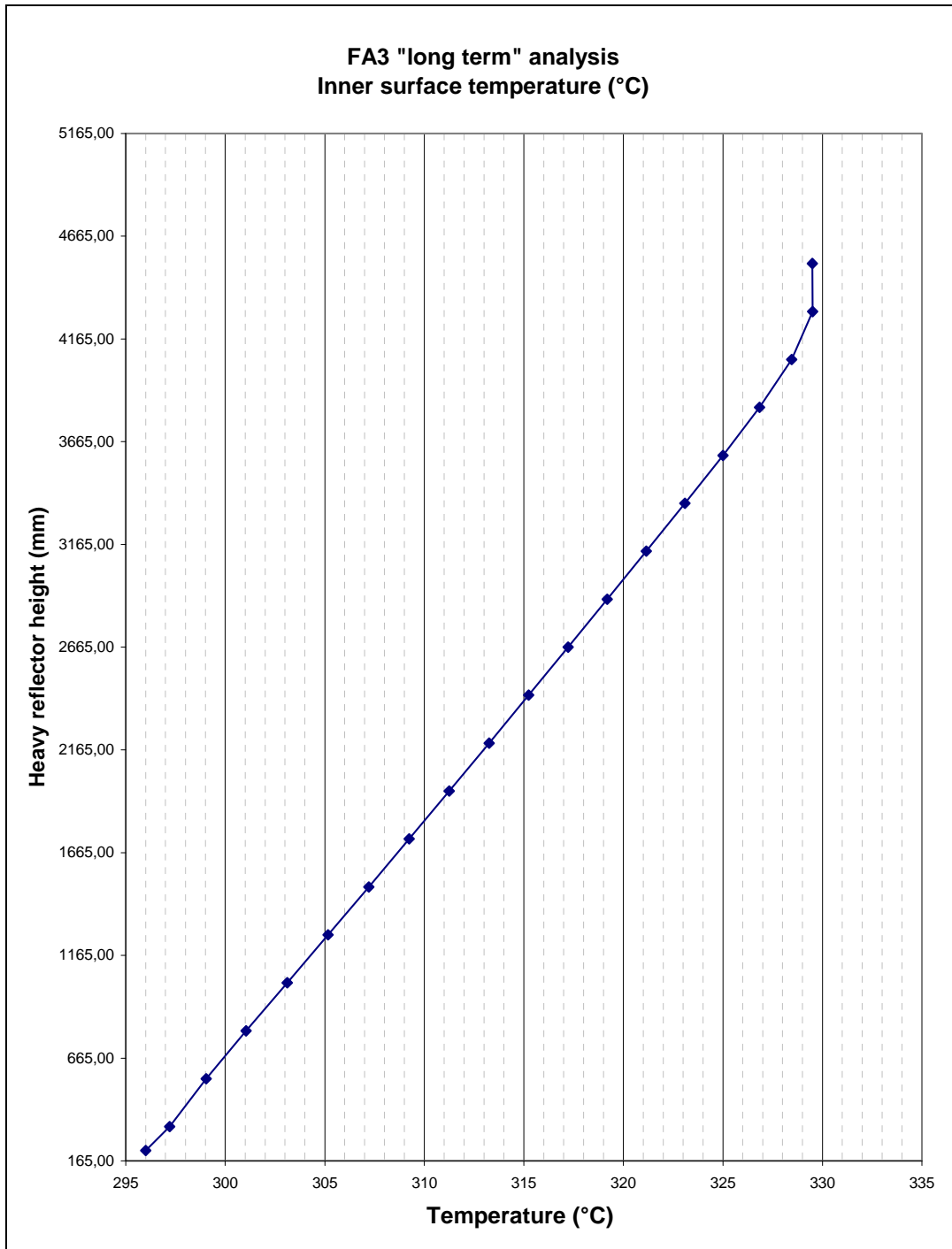


Figure.3.11: Inner Wall Free Stream Temperature Profile

For $0 \text{ mm} < y < 3600 \text{ mm}$

$$T = \frac{29.1}{3400}(1000 y - 200) + 295.9$$

For $3600 \text{ mm} < y < 4000 \text{ mm}$

$$T = \frac{3}{400}(1000 y - 3600) + 325$$

For $4000 \text{ mm} < y < 4300 \text{ mm}$

$$T = 0.005(1000 y - 4000) + 328$$

For $4300 < y$

$$T = 329.5$$

y is the height measured from the bottom of Slab I in meters.

Figure 3.12: The Curve Fit Equations Used to Implement the Temperature Profile in Figure 3.11 into FLUENT

3.7 Results

The resulting temperature distribution is shown in the Figure 3.13 and 3.14 on the next page. The contour in Figure 3.13 shows the temperature distribution at the planes between the slabs. Figure 3.14 shows the temperature profile at the height where the temperature is the highest. As shown in the figures, the highest temperature is in Slab X, and its magnitude is about 347.7 °C, which is below the maximum allowable temperature. Note that the temperature is higher near the core than it is near the outer surface region. For this reason, the heat transfer along the inner wall is more important than that of the outer wall. Since the heat transfer coefficient on the inner wall is set very high, it is possible that it is causing too much cooling on this wall. Therefore, an additional calculation is conducted with a lower heat transfer coefficient. The heat transfer coefficient used in this calculation is a half of the original value; however, the increase in the maximum temperature turns out to be only 1 °C. This is still below the allowable temperature. Consequently, it is concluded that the criteria for the maximum temperature is met without any modification in the flow distribution of the coolant.

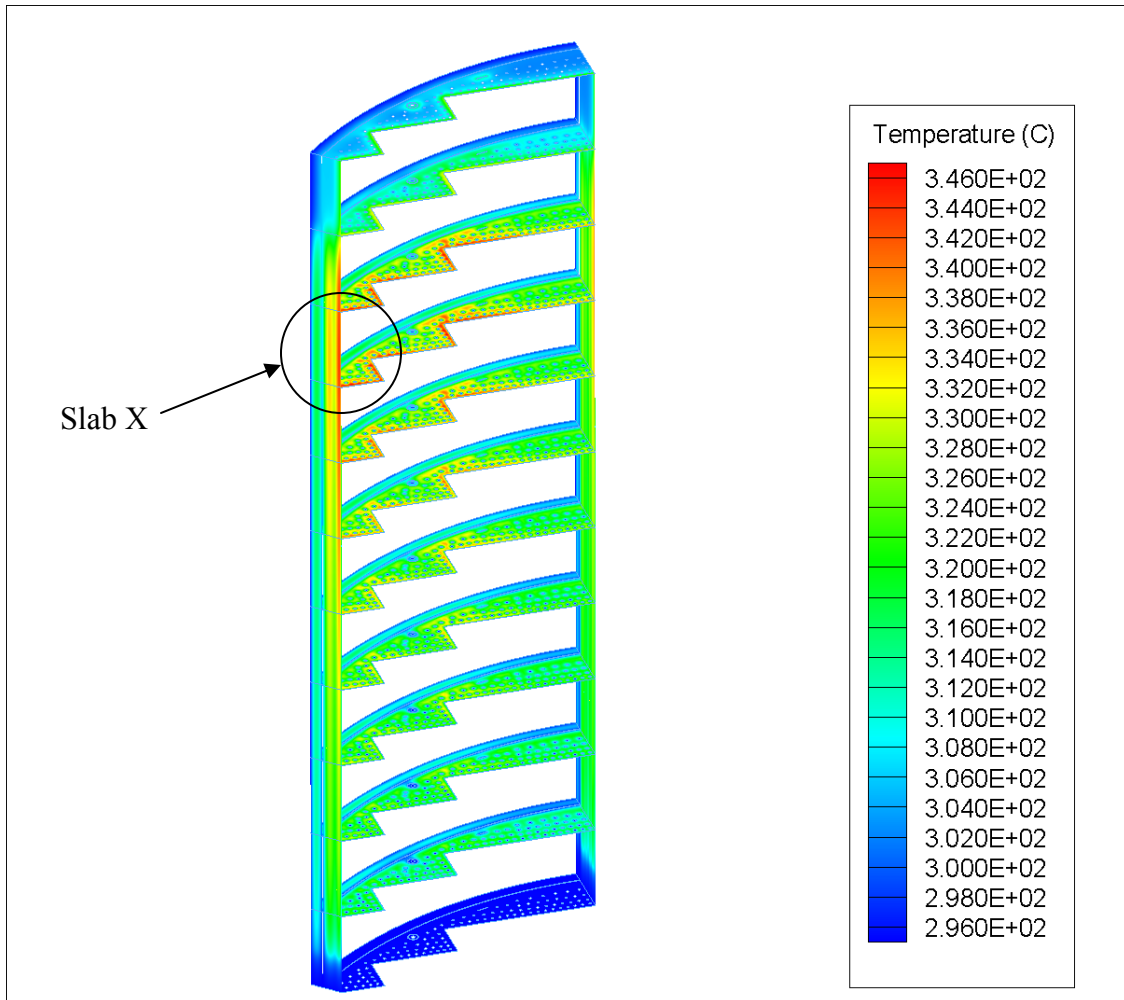


Figure 3.13: Isometric View of the Temperature Distribution

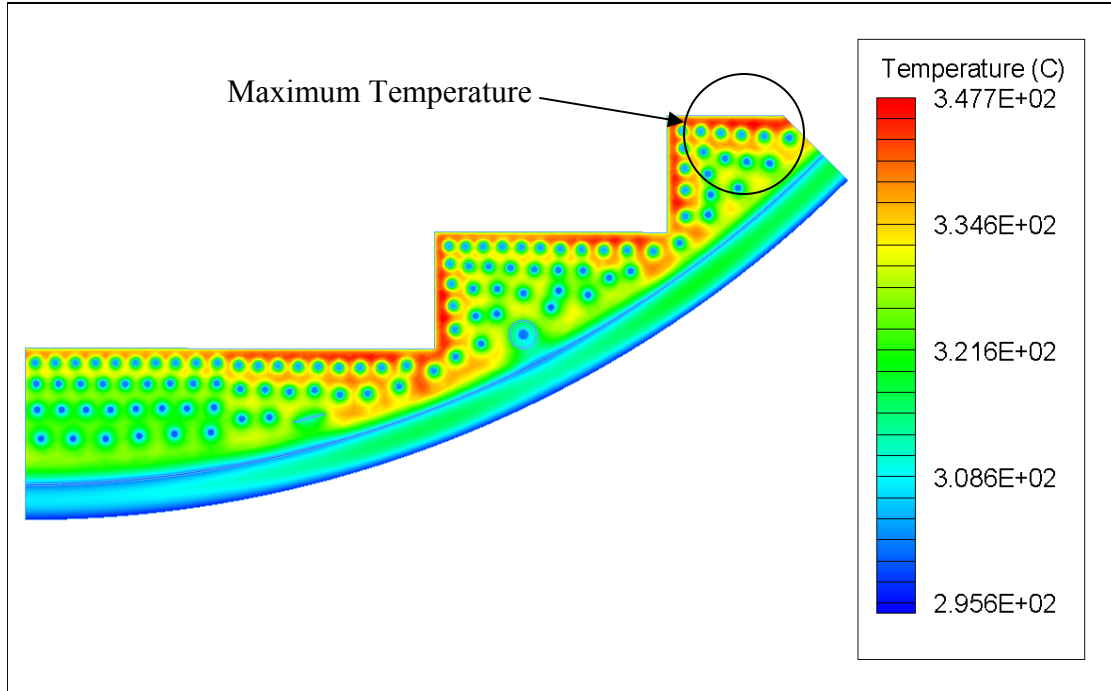


Figure 3.14: Top View of the Temperature Distribution in Slab X

3.8 Flow Rate Sensitivity Study

A few additional studies are conducted to determine the margin of maximum temperature by adjusting the flow rates in the cooling channels. In these studies, more flow is concentrated in the cooling channels in the region where the temperature is high so that more heat is extracted from this region. The flow rates in these cases are calculated using the flow distribution model in the previous chapter. The orifices are removed from those channels where the higher flow rate is desired, and the resulting flow rates are recorded. Although there are some variations in the flow rates among those channels, the average of those flow rates is used for the heat transfer calculation. The lowest maximum temperature achieved through this study is about 345.7 °C with 35 channels without orifices, as shown in Figure 3.15.

The channels with the lower temperatures are the ones with the higher flow rate. The flow rate for these channels is 0.326 kg/s while that of other channels is 0.130 kg/s. Even with this much variation in the flow rate, the resulting maximum temperature 345.7

°C is not too much lower than 347.7 °C from the uniform flow distribution case. Since the flow rate 0.326 kg/s is more than 1.5 times the original flow rate, 0.196 kg/s, this small reduction in the maximum temperature is a little unexpected. For this reason, a quick test is conducted to see the effect of increasing the flow rate in the cooling channels. In this calculation, the orifices are taken away from only six channels in the region where the maximum temperature is located. This gives these channels a flow rate of 0.417 kg/s, which is more than twice the original flow rate. However, the maximum temperature in this given region turns out to be about 344.8 °C, which is only about 3 °C lower than the original case. This leads to a conclusion that the resulting temperature is not significantly sensitive to the change in flow rate in the cooling channels. This is probably caused by the heat generation in the hot region being high enough that the convection heat transfer associated with the cooling channels in this region cannot make much difference within the given range of flow rate. Lowering the maximum temperature in the heavy reflector would require a significant change in the total flow rate rather than a simple redistribution of the flows in the channels.

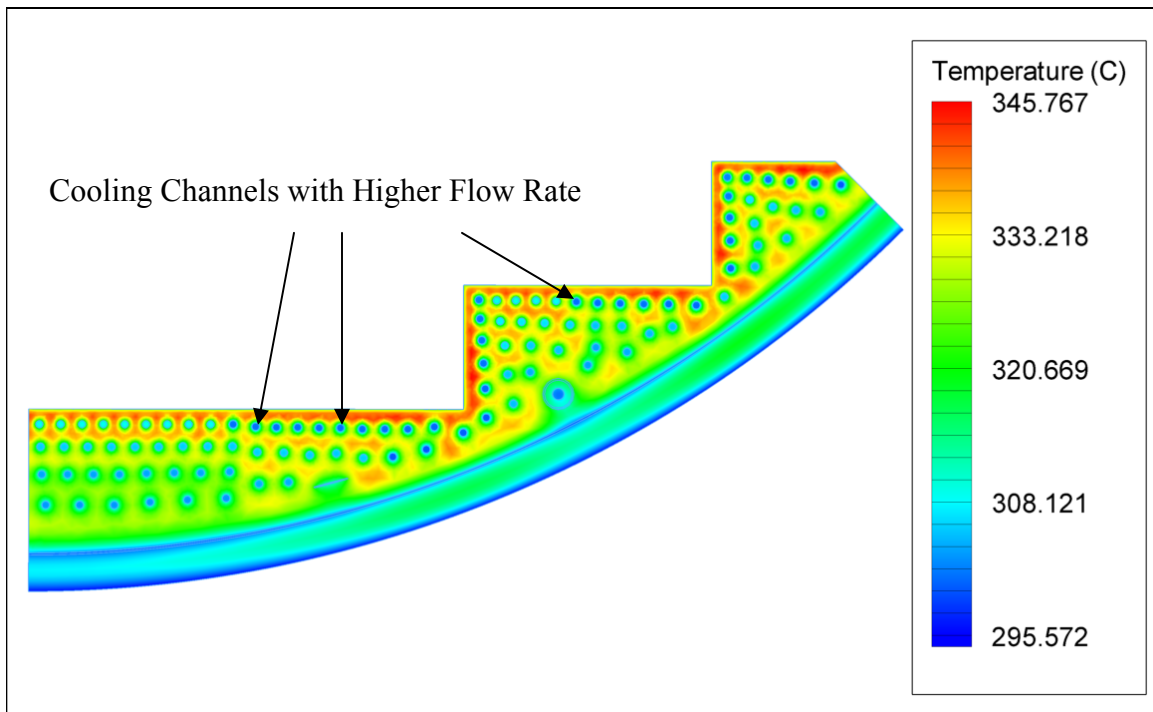


Figure 3.15: Temperature Distribution with 35 Channels without Orifices

CHAPTER 4. SUMMARY AND CONCLUSION

The temperature distribution in the U.S. EPR™ heavy reflector was investigated using a commercial CFD code, FLUENT. In order to perform the heat transfer analysis, the flow distribution of the coolant in the cooling channels was first calculated to test for any maldistribution. In order to reduce the computational cost for this calculation, a simplification method using the “equivalent flow resistance” was developed. This method was validated by running a few case studies. Using this method, the calculation only required the first and the second slabs of the heavy reflector. The results of the calculation showed that the difference in the maximum and the minimum flow rates in the cooling channels is only 3.47 %; therefore, it was concluded that there is no significant maldistribution of the coolant.

The temperature distribution was found by calculating the conjugate heat transfer in the heavy reflector. Due to the nature of the problem, the simplification method used in the flow distribution calculation does not apply to the computational model for this calculation, and a total of eleven slabs in the heavy reflector had to be modeled. In order to reduce the computational cost of this calculation, a grid sensitivity study was conducted on the fluid region of the model to determine the minimum grid density that gives accurate results in heat transfer calculation. Using the results from the study, a computational grid with a total of about 9 million cells was generated. The heat source for the problem was also discussed and was implemented in FLUENT using a set of custom functions called UDF. The resulting temperature distribution showed that the maximum temperature in the heavy reflector, with uniform flow distribution in the cooling channels, is 347.7 °C while the maximum allowable temperature is 350 °C. The maximum temperature in the heavy reflector is below the maximum allowable temperature, though not by much, and there is no need for modification of the flow distribution in the cooling channels.

A few additional calculations were conducted to test the sensitivity of the maximum temperature with change in flow rates in the cooling channels. The new flow rates were determined by simply redistributing the coolant flow, concentrating more flow in the region with high temperature. The results showed that the maximum temperature in the heavy reflector does not change significantly with the change in the flow rates in the cooling channels. The heat generation in the hot region is too high compared to the convective heat transfer associated with the cooling channels, and the maximum temperature in the heavy reflector cannot be reduced by much without a significant change in the total flow rate.

References:

- 1. AREVA Document. "U.S. EPR™ Brochure." AREVA. (2007)**
- 2. AREVA Document NEER-F DC 129 A BPEEN-REF HR. "RPV Internals Mechanical Dimensioning/Heavy Reflector/Design Validation-CAT 1 & 2" AREVA. (2007)**
- 3. Jones, Stuart. "US EPR DC Steady-State RPV Hydraulics FATHOM Model 32-9017576-001" AREVA. (2007)**
- 4. White, Frank M. "Fluid Mechanics Fifth Edition" McGraw-Hill Companies, Inc. New York. (2003)**
- 5. Touna, M. L. "U.S. EPR Design Certification Project Heavy Reflector Assembly Drawing" AREVA. (2007)**
- 6. Touna, M. L. "U.S. EPR Design Certification Project RPV Internals Lower Slab" AREVA. (2007)**
- 7. Touna, M. L. "U.S. EPR Design Certification Project RPV Internals Typical Slab" AREVA. (2007)**
- 8. "Fluent 6.3 User's Manual" Fluent, Inc. (2006)**
- 9. Gielinski, V. "Forced Convection in Ducts" in "Hemisphere Handbook of Heat Exchanger Design" ed. G.F. Hewitt. Section 2.5.1. Hemisphere Publishing Corporation. New York. (1990)**
- 10. Yee, Norman S. "US EPR Heavy Reflector Temperatures 32-9052000-000" AREVA. (2007)**
- 11. Byard, J. N. "US EPR Heavy Reflector Gamma Heating Calculation 32-9037276-001" AREVA. (2007)**
- 12. Wilcox, David. "Turbulence Modeling for CFD Third Edition" DCW Industries, Inc. California. (2006)**
- 13. Incropera, F., Dewitt D., Bergman T., and Lavine A. "Fundamentals of Heat and Mass Transfer Sixth Edition" John Wiley & Sons, Inc. New Jersey. (2007)**

Appendix A Basic Equations

The basic equations solved in FLUENT for this CFD analysis include conservation in mass or continuity, momentum, and energy. For a steady turbulent incompressible flow the equations are

$$\text{Continuity:} \quad \frac{\partial \bar{u}_i}{\partial x_i} = 0 \quad (\text{A.1})$$

$$\text{Momentum:} \quad \rho \bar{u}_j \frac{\partial \bar{u}_i}{\partial x_j} = -\frac{\partial P}{\partial x_i} + \frac{\partial}{\partial x_j} \left(\mu \frac{\partial \bar{u}_i}{\partial x_j} - \rho \overline{u'_i u'_j} \right) + \rho g_i \quad (\text{A.2})$$

$$\text{Energy:} \quad \rho c_p \bar{u}_j \frac{\partial \bar{T}}{\partial x_j} = \frac{\partial}{\partial x_j} \left(k \frac{\partial \bar{T}}{\partial x_j} - \rho c_p \overline{u'_j T'} \right) \quad (\text{A.3})$$

where u is the velocity, u' is the fluctuating component of u , P is the pressure, μ is the viscosity, T is the temperature, T' is the fluctuating component of T , k is the thermal conductivity, ρ is the density, and c_p is the specific heat. Note that the energy equation does not include any viscous dissipation, pressure work, and kinetic energy terms. These terms are often negligible in incompressible flow; therefore, FLUENT does not include them by default. Also note that all variables with a bar are time averaged using Reynolds averaging, which is defined as

$$\bar{\phi} = \lim_{t \rightarrow \infty} \frac{1}{t} \int_0^t \phi(x_i, t) dt \quad (\text{A.4})$$

where

$$\phi = \bar{\phi} + \phi' \quad (\text{A.5})$$

In these equations, ϕ is the variable of interest, ϕ' is the fluctuating component, and t is the period over which the variable is averaged. The solid region has no motions involved, so the energy equation simply becomes

$$k \frac{\partial^2 T}{\partial x_j^2} + S = 0 \quad (\text{A.6})$$

where S is the source term, which is the heat generation due to absorption of the gamma radiation.

Appendix B Turbulence Model

The average Reynolds numbers for all the modeled flow paths indicate that the flows through all of these flow paths are turbulent. In turbulent flows, the equations for conservation of momentum and energy have extra terms that involve the fluctuation of the velocity and the temperature as shown in Equations (A.2) and (A.3). In order to solve for these fluctuation terms, CFD codes often use what is called turbulence models. One of the most common methods used in turbulence models to approximate the fluctuation term in the momentum equation, $-\rho\overline{u'_i u'_j}$, is called Boussinesq approximation. Boussinesq approximation states

$$\tau_{ij} = 2\nu_T S_{ij} - \frac{2}{3} k \delta_{ij} \quad (\text{B.1})$$

where τ_{ij} is the Reynolds-stress tensor, ν_T is the kinematic eddy viscosity, S_{ij} is the strain-rate tensor, and k is the turbulence kinetic energy. The Reynolds-stress tensor is defined as the following.

$$\tau_{ij} = -\overline{u'_i u'_j} \quad (\text{B.2})$$

The equation governing the turbulence kinetic energy is

$$\bar{u}_j \frac{\partial k}{\partial x_j} = \tau_{ij} \frac{\partial \bar{u}_i}{\partial x_j} - \varepsilon + \frac{\partial}{\partial x_j} \left[\left(\nu + \frac{\nu_T}{\sigma_k} \right) \frac{\partial k}{\partial x_j} \right] \quad (\text{B.3})$$

where ε is the dissipation, ν is the kinematic viscosity, and σ_k is a constant. The main focus of this appendix is on a turbulence model called k- ε model because it is the model used in this project.

B.1 k- ε Model

k- ε model is one of the most common turbulence models used in CFD. It is applicable to a wide range of industrial problems and is relatively less computationally expensive than most of the other turbulence models. The standard k- ε model assumes that the flow is fully turbulent, and the turbulent kinetic energy and the dissipation are solved

using Equations (B.1), (B.3), (B.4), and (B.5).

$$\bar{u}_j \frac{\partial \varepsilon}{\partial x_j} = C_{\varepsilon 1} \frac{\varepsilon}{k} \tau_{ij} \frac{\partial \bar{u}_i}{\partial x_j} - C_{\varepsilon 2} \frac{\varepsilon^2}{k} + \frac{\partial}{\partial x_j} \left[\left(\nu + \frac{\nu_T}{\sigma_\varepsilon} \right) \frac{\partial \varepsilon}{\partial x_j} \right] \quad (\text{B.4})$$

$$\nu_T = C_\mu \frac{k^2}{\varepsilon} \quad (\text{B.5})$$

where $C_{\varepsilon 1}$, $C_{\varepsilon 2}$, C_μ , and σ_ε are coefficients determined experimentally. The default values of these coefficients in FLUENT are the followings.

$$C_{\varepsilon 1} = 1.44 \quad C_{\varepsilon 2} = 1.92 \quad C_\mu = 0.09 \quad \sigma_k = 1.0 \quad \sigma_\varepsilon = 1.3$$

The fluctuation term in the energy equation, $-\rho c_p \overline{u'_j T'}$, is approximated by

$$-\rho c_p \overline{u'_j T'} = \rho c_p \frac{\nu_T}{Pr_t} \frac{\partial \bar{T}}{\partial x_j} \quad (\text{B.6})$$

where Pr_t is the turbulent Prandtl number, which is set to 0.85 by default. There are also some improved versions of k- ε models available in FLUENT. The flow field calculation in Chapter 2 uses RNG k- ε model, which has an extra term added to the dissipation equation in the standard k- ε model and is applicable to some lower Reynolds number flows in addition to the fully turbulent flow that standard version covers. For more details see References [8] and [12].

B.2 Near Wall Treatment and Y-plus

In wall-bounded turbulent flow problems, the existence of walls affects the flow significantly, especially near walls. The turbulence models are designed to calculate the flow field away from the wall. Therefore, the flow field near walls has to be calculated using another method. The region near walls consists of three layers: viscous sublayer, buffer layer, and fully-turbulent layer. Viscous sublayer is the closest to the wall, and the fluid velocity in this layer is very slow due to the non-slip condition at the wall. Consequently, the viscosity effects dominate in determining the flow field in this layer. Fully-turbulent layer is the layer farthest from the wall, where the fluid velocity becomes faster, and turbulence determines the flow. Buffer layer is simply the layer between the viscous sublayer and the fully-turbulent layer where both viscosity and turbulence

determine the flow characteristics. The general locations of these layers can be described in terms of the distance from the wall using a non-dimensional variable called y-plus. Y-plus is similar to Reynolds number in its definition, but the velocity used in this variable is what is called friction velocity, and the length scale is the distance from the wall instead of the diameter. So the equation for y-plus is

$$y^+ = \frac{\rho u_\tau y}{\mu} \quad (\text{B.7})$$

where y is the distance from the wall and u_τ is the friction velocity. u_τ is a function of wall shear and density and is defined as the following.

$$u_\tau = \sqrt{\frac{\tau_w}{\rho}} \quad (\text{B.8})$$

τ_w is the wall shear. The wall shear is a function of Darcy friction factor, which is dependent on the Reynolds number. In other words, the y-plus is a non-dimensionalized distance from the wall that is based on Reynolds number and the physical distance. More details can be found in Reference [12]. Viscous sublayer is generally in the range of $0 < y^+ < 5$, which can be around 1/1000 of a millimeter in scale or even smaller, depending on the Reynolds number. Buffer layer is around $5 < y^+ < 60$, and the fully-turbulent layer is the rest. FLUENT provides two different approaches to solve the flow field in these layers near walls. One approach is the near-wall modeling, where the flow field is resolved all the way to the wall using a very fine grid. However, viscous sublayer is so close to the wall that it requires the mesh near walls to be extremely fine; consequently, this method can make the calculation computationally very expensive. Another approach is called the wall function method. The wall functions use semi-empirical equations to approximate the flow in the near-wall region and relate the resulting data to the flow far from the wall. Since this method does not require as fine of a mesh near walls, it is relatively less computationally expensive than the near-wall modeling method. One of the semi-empirical equations used in wall functions is called the law of the wall. The law of the wall states

$$u^+ = \frac{1}{\kappa} \ln(y^+) + C \quad (\text{B.9})$$

where

$$u^+ = \frac{u}{u_\tau} \quad (\text{B.10})$$

where u is the velocity. From experiments, the constants are determined to be $\kappa = 0.41$ and $C = 5.0$ for flows along smooth walls, though different CFD codes may use slightly different values. The flow velocity at the first grid point from the wall can be determined using this equation, and the rest of the flow field can be solved using the turbulence model.

Appendix C Definition of Pressure in FLUENT

The definition of pressure in FLUENT is a modified pressure. Instead of using a regular gauge pressure, FLUENT subtracts the hydrostatic pressure. So the redefined pressure is

$$P' = P - \rho_o \bar{g} \cdot \bar{x} \quad (C.1)$$

where P is the actual gauge pressure including the hydrostatic pressure, ρ_o is a reference density called operation density, \bar{g} is the gravity force vector, and \bar{x} is the distance vector from the reference point. Now consider the general momentum equation

$$\rho \frac{D\bar{V}}{Dt} = -\nabla P + \rho \bar{g} + \nabla \cdot \bar{\tau} \quad (C.2)$$

By adding and subtracting the $\rho_o \bar{g} \cdot \bar{x}$ term, the pressure gradient term becomes

$$\begin{aligned} \nabla P &= \nabla(P - \rho_o \bar{g} \cdot \bar{x} + \rho_o \bar{g} \cdot \bar{x}) = \nabla(P - \rho_o \bar{g} \cdot \bar{x}) + \rho_o \bar{g} \\ &\Rightarrow \nabla P' + \rho_o \bar{g} \end{aligned} \quad (C.3)$$

Substituting Equation (C.3) into Equation (C.2), the momentum equation then becomes

$$\begin{aligned} \rho \frac{D\bar{V}}{Dt} &= -\nabla P' - \rho_o \bar{g} + \rho \bar{g} + \nabla \cdot \bar{\tau} \\ &\Rightarrow \rho \frac{D\bar{V}}{Dt} = -\nabla P' + (\rho - \rho_o) \bar{g} + \nabla \cdot \bar{\tau} \end{aligned} \quad (C.4)$$

For incompressible flows, $\rho = \rho_o$, so the term $(\rho - \rho_o) \bar{g}$ in Equation (C.4) becomes zero. FLUENT uses this technique to avoid numerical errors and thus speed up the convergence of the calculation. However, this means the pressure FLUENT displays in the calculation results is the modified pressure P' instead of the actual gauge pressure P . There are two different ways to find the actual gauge pressure P : simply calculate the hydrostatic pressure and add it to P' , or set the operation density to zero so that all the modified terms become the same as the regular values, making Equation (C.4) back to Equation (C.2). In the flow distribution analysis conducted in Chapter 2, the operation density is set to zero so that the pressure values are more easily compared with other analysis.

Appendix D Determining K_o for the Orifices in the Heavy Reflector

The loss coefficient K_{eq} that is used in the outlet vent condition at the outlet of the cooling channels in the flow distribution calculation has to include the friction term, which is calculated using an estimated average fluid velocity as discussed in the section 2.3, and the loss coefficient associated with the orifices K_o . Orifices are located at the bottom of the channels in each slab of the reflector as shown in Figure 2.2. So each channel, drilled through Slabs II through XII, has a total of eleven orifices. The first orifice is included in the computational model since it is the entrance of the channel; however, the remaining ten are not included in the grid. Consequently, K_o has to include all of these ten orifices. In order to calculate this value, the loss coefficient per orifice is calculated. K_o is simply ten times this loss coefficient per orifice.

D.1 Theoretical Value

The loss coefficient per orifice is calculated using CFD calculations; however, the theoretical value of the loss coefficient is first calculated for comparison purpose. The flow through an orifice experiences two separate losses, sudden contraction from the slab below into the orifice and sudden expansion out from the orifice. Although the sudden expansion is angled 30 degrees instead of having a sharp, 90 degrees edge, the length of the angled portion is short enough that it is assumed to be a sudden expansion rather than a gradual expansion such as a diffuser. The diameters of the channel and the orifice are 13 mm and 8 mm, respectively. The head loss due to the sudden contraction or the sudden expansion is given by

$$h = K \frac{V^2}{2g} \quad (D.1)$$

where h is the head loss, K is the loss coefficient, and V is the mean fluid velocity in the region with smaller diameter. According to Reference [4], the values of K associated with the sudden contraction and the sudden expansion with the given diameter ratio are 0.261

and 0.386, respectively. Note that these values are based on the fluid velocity in the region with smaller diameter, which is the orifice. Since the velocity in Equation (2.6) is the mean fluid velocity in the channel instead of the orifice, the loss coefficient in Equation (D.1) has to be corrected to the value corresponding to this velocity. The relationship between the fluid velocity in the regions with a smaller and a larger diameter is the following:

$$A_S V_S = A_L V_L \quad (D.2)$$

where A_S and V_S are the area and the velocity in the region with a smaller diameter, and A_L and V_L are those for the region with a larger diameter. Since both the channels and the orifices are cylindrical, both areas are functions of the diameter in each region, and Equation (D.2) can be rewritten as the following:

$$V_S = \left(\frac{D_L}{D_S} \right)^2 V_L \quad (D.3)$$

where D_S and D_L are the diameters in the regions with a smaller diameter and the region with a larger diameter, respectively. Substituting Equation (D.3) into Equation (D.1) yields

$$h = \frac{1}{2g} K (V_S)^2 = \frac{1}{2g} \underbrace{\left(K \left(\frac{D_L}{D_S} \right)^4 \right)}_{K_L} (V_L)^2 \quad (D.4)$$

where K_L is the loss coefficient associated with V_L . Consequently, the K values 0.261 and 0.386 are equivalent to the K_L values 1.82 and 2.69, respectively, for the given combination of the diameters. Simply adding the two, the theoretical value of the loss coefficient for the flow going through an orifice becomes 4.67.

D.2 Computation of K_o in FLUENT

The loss coefficient K_o is calculated by comparing the pressure drop in the flow through a given length of the channel with and without an orifice. For the flow through the channel without an orifice, the data is taken from Case 1 discussed in section 2.4.3. The channel with an orifice is modeled as shown in Figure D.1. The difference in the

pressure drop in the flow through the channels with and without the orifice is equal to the pressure drop associated with the head loss due to the fluid flowing through the orifice. This pressure drop associated with the head loss is given by

$$\Delta P = K \frac{1}{2} \rho V^2 \quad (D.5)$$

where K is the loss coefficient per channel, ρ is the density, and V is the velocity of the fluid in the channel. The K and V here correspond to K_L and V_L in Equation (D.4). Solving Equation (D.5) for K gives the loss coefficient per orifice. The results are shown in Table D.1.

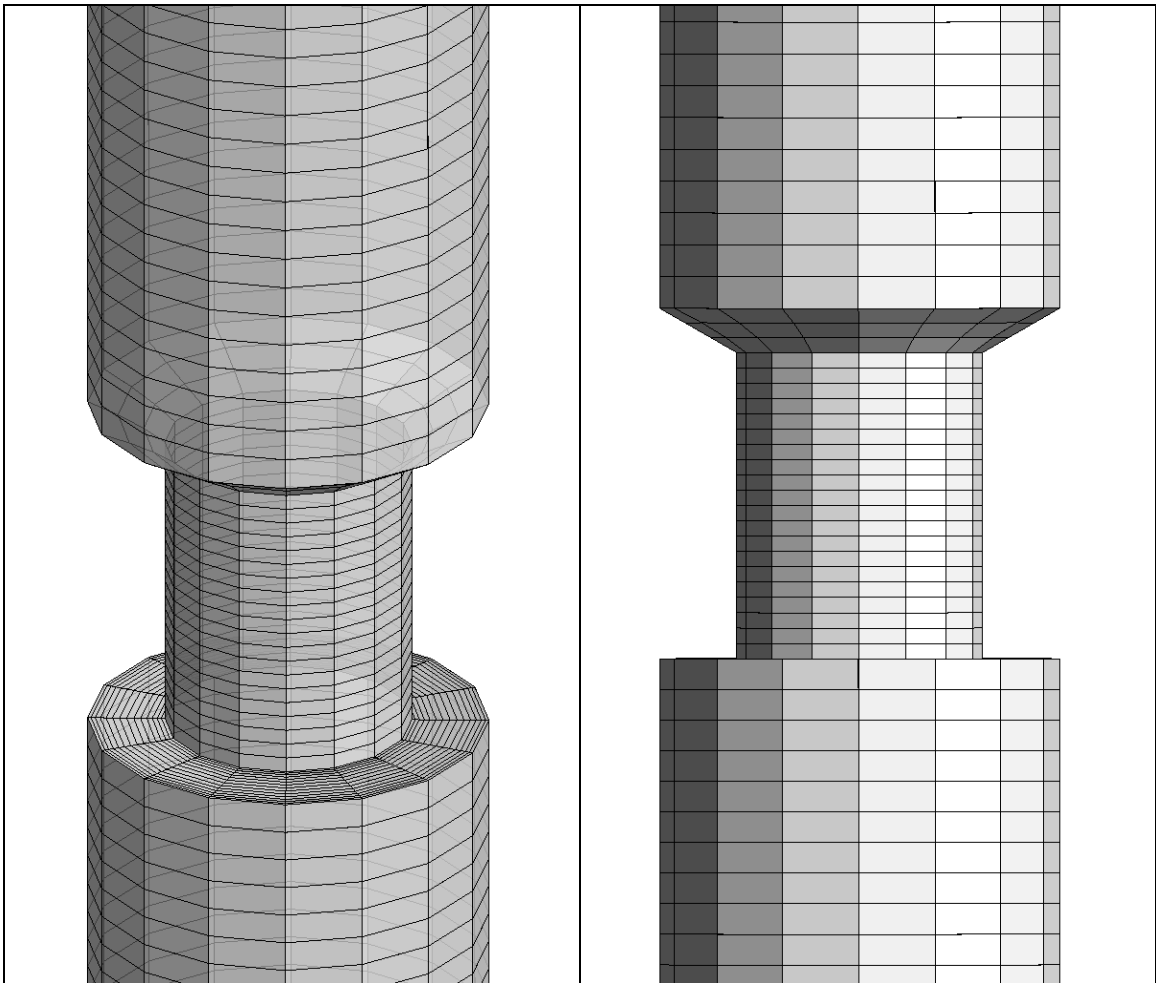


Figure D.1: Orifice Grid

Table D.1: K Value for an Orifice

Measured Length (mm)	400
Pressure Drop without an Orifice (Pa)	3514
Pressure Drop with an Orifice (Pa)	13514
Change in Pressure Drop (Pa)	9990
Average Fluid Velocity in the Channel (m/s)	2.23
Equivalent Loss Coefficient per Orifice	5.79

The value 5.79 is greater than the theoretical value 4.67. Recall that the theoretical value was found by calculating the loss coefficients for the sudden contraction and expansion are calculated separately. The equations used to calculate these values [4] are based on the assumption that the flow in the upstream of the contraction or expansion is fully-developed. For the given length of orifice, however, the flow does not become fully developed within the region between the contraction and the expansion. For this reason, the loss coefficient through an orifice is expected to be different from the value 4.67, though should be in a similar range. This explains the difference between the theoretical value and the value calculated from the CFD calculation. K_o that is included in the flow distribution calculation is ten times the obtained value of loss coefficient per orifice; therefore, $K_o = 57.9$.

Appendix E Equations and Correlations for Grid Sensitivity Study

The flow is turbulent in all of the flow paths analyzed in the grid sensitivity study. While the dimensions used in each flow path is taken from the actual geometry, the heat transfer problem is simplified for the purpose of the study by studying each flow path with a constant surface temperature. Since internal flows with a constant surface temperature have been studied for many years, there are several known correlations that can be used to determine the theoretical values to compare with the CFD solutions. The correlations used in this study are the following:

$$\text{Dittus-Boelter:} \quad \overline{\text{Nu}} = 0.023 \text{ Re}^{0.8} \text{ Pr}^{0.4} \quad (\text{E.1})$$

$$\text{Gnielinski (Fully-Developed):} \quad \overline{\text{Nu}} = 0.0214 (\text{Re}^{0.8} - 100) \text{ Pr}^{0.4} \quad (\text{E.2})$$

$$\text{Gnielinski (Developing):} \quad \overline{\text{Nu}} = 0.0214 (\text{Re}^{0.8} - 100) \text{ Pr}^{0.4} [1 + (D/L)^{2/3}] \quad (\text{E.3})$$

In these equations, $\overline{\text{Nu}}$ is the average Nusselt number, Re is the Reynolds number, Pr is the Prandtl number, D is the diameter, and L is the length of the flow path in the axial direction. Equation (E.1) is the Dittus-Boelter correlation for fully developed turbulent flows and applies only to the fully developed region [13]. Equations (E.2) and (E.3) are the correlations suggested by Gnielinski [9]. Equation (E.2) is also for fully developed region. Equation (E.3) has a correction term to account for the effect of the entrance region and may be applied to any region within $0 < D/L < 1$ range, which includes the developing region. Both Equation (E.2) and (E.3) are for $0.5 < \text{Pr} < 1.5$. Although Gnielinski's correlations do not match up perfectly with Dittus-Boelter correlation in the fully developed region, Equation (E.3) is used for the region with flow development because Dittus-Boelter correlation does not account for the effect of the entrance region. The non-dimensional parameters, Nu, Re, and Pr are defined as the following:

$$\overline{\text{Nu}} = \frac{\overline{h}D}{k} \quad (\text{E.3})$$

$$\text{Re} = \frac{uD}{\nu} \quad \text{where} \quad \nu = \frac{\mu}{\rho} \quad (\text{E.4})$$

$$\text{Pr} = \frac{\nu}{\alpha} \quad (\text{E.5})$$

where \bar{h} is the average heat transfer coefficient, k is the conductivity of the fluid, u is the average velocity in the flow direction, ν is the kinematic viscosity, ρ is the density, μ is the dynamic viscosity, and α is the thermal diffusivity. Since some of the flow paths in the study are not simple circular tubes, the hydraulic diameter D_h is used instead of the regular diameter D . D_h is defined as the following:

$$D_h = \frac{4A_c}{P} \quad (E.6)$$

where A_c is the cross sectional area and P is the wetted perimeter. The heat transfer coefficient, h , corresponding to Equations (E.1) and (E.2) are found by simply solving Equation (E.3) for h , which becomes

$$\bar{h} = \overline{Nu} \frac{k}{D} \quad (E.7)$$

Substituting Equations (E.1), (E.2), and (E.3), the equations for the average heat transfer coefficient for the fully developed region become Equation (3.1) and (3.2), and that for the developing region becomes Equation (3.3). These values are then compared with the average heat transfer coefficient found from the CFD calculation results. The average heat transfer coefficient from the CFD calculation is determined using the following equation found in Reference [13]:

$$\frac{T_s - T_m(x)}{T_s - T_{m,i}} = \exp\left(-\frac{Px}{\dot{m}c_p} \bar{h}\right) \quad (E.10)$$

where x is the location in the flow path measured from the inlet in the flow direction, \dot{m} is the mass flow rate, c_p is the specific heat, T_s is the surface temperature, $T_m(x)$ is the mean fluid temperature at x , and $T_{m,i}$ is the mean fluid temperature at the inlet. Solving this equation for \bar{h} results in the following:

$$\bar{h} = -\frac{\dot{m}c_p}{Px} \ln\left(\frac{T_s - T_m(x)}{T_s - T_{m,i}}\right) \quad (E.11)$$

Note that theoretical values from Equations (3.1), (3.2), and (3.3) have some uncertainty associated with them, due to the uncertainty associated with Equations (E.1), (E.2), and (E.3) which is up to 20 %. For this reason, the value of \bar{h} from CFD calculation is not expected to be exactly the same as the theoretical values; however, they should be in a similar range.

Appendix F Data Format for Interpolation in FLUENT

2 (FLUENT version: 1 for FLUENT 5, 2 for FLUENT 6)
3 (Dimensions: 2 for two-dimensional, 3 for three-dimensional)
n (number of points in each dimension)
1 (number of variables)
uds-0 (name of the variable; it has to agree with the name defined in UDS panel.)
x1 (data point locations in x-coordinate)
x2
x3
:
xn
y1 (data point locations in y-coordinate)
y2
y3
:
yn
z1 (data point locations in z-coordinate)
z2
z3
:
zn
v1 (value of the variable at the data point)
v2
v3
:
vn

Appendix G

MATLAB Code for Heat Generation Data Conversion

```
clear all;

%read 2D data file (coordinates are in mm, q is in W/cm3)
fid=fopen('gammarad.txt','r');
scan=fscanf(fid,'%g %g %g',[3,inf]);
x=scan(1, :);
z=scan(2, :);
q=scan(3, :);
fclose(fid);

%convert units of heat source from W/cm3 to W/m3
%factor
n=length(q);
for i=1:n
    q(i)=q(i)*1000000;
end

%define y
ymax=417*11;
y=0 :5.5 :ymax;

m=length(y);

%convert y from mm to cm for axial factor calculation
for i=1:m
    yy(i)=y(i)/10;
end
```

```

%create vector for 3D heat source data
t=n*m ;
g=zeros(t,1) ;

for i=1:m
    h=yy(i)+16.5;
    if h<35
        fy=(1.2277446e-3)*exp((1.7027242e-1)*h);
    elseif h<100
        fy=-((1.0207128e-7)*h^4+(3.0540065e-5)*h^3-(3.4369916e-3)*h^2+(1.7628381e-1)*h-(2.5361444e0));
    elseif h<352
        fy=(2.9378111e-4)*h+(1.0239436e0);
    elseif h<440
        fy=-((4.9187099e-8)*h^4+(7.4042207e-5)*h^3-(4.1831106e-2)*h^2+(1.0509929e1)*h-(9.8948889e2));
    else
        fy=(4.8495796e21)*exp(-(1.1926225e-1)*h);
    end
    for j=1:n
        g((i-1)*n+j)=q(j)*fy;
    end
end

fid2=fopen('3dgamma2.ip','w');
fprintf(fid2,'2\n');
fprintf(fid2,'3\n');
fprintf(fid2,'%7.0f\n',t) ;
fprintf(fid2,'1\n');
fprintf(fid2,'uds-0\n');

```

```
%print x-coordinates in m
for i=1:m
    for j=1:n
        fprintf(fid2,'%f\n',x(j)/1000);
    end
end

%print y-coordinates in m
for i=1:m
    for j=1:n
        fprintf(fid2,'%f\n',y(i)/1000);
    end
end

%print z-coordinates in m
for i=1:m
    for j=1:n
        fprintf(fid2,'%f\n',z(j)/1000);
    end
end

%print g
for i=1:t-1
    fprintf(fid2,'%g\n',g(i));
end
fprintf(fid2,'%g',g(t));

fclose(fid2);
```

Appendix H

UDF Code from ANSYS Online Technical Support

DEFINE_ON_DEMAND function is a type of UDF that can be run anytime while there is no iteration running. This is used to copy the data in UDS to UDM. DEFINE_SOURCE function lets the user to set a UDF, in this case UDM, as the source term in boundary conditions. The sections of the code with DEFINE_ON_DEMAND and DEFINE_SOURCE commands are taken from the ANSYS Online Technical Support. The section with DEFINE_PROFILE is written by the author.

```
#include "udf.h"

DEFINE_ON_DEMAND(copy_uds_to_udm)
{
  Domain* d = Get_Domain(1);
  Thread* t;
  cell_t c;
  thread_loop_c(t,d)
  {
    begin_c_loop(c,t)
    {
      C_UDMI(c,t,0) = C_UDSI(c,t,0);
    }
    end_c_loop(c,t);
  }
  return;
}

DEFINE_SOURCE(my_source,c,t,dS,eqn)
{
```

```

real source;
dS[eqn] = 0.0;
source = C_UDMI(c,t,0);
return source;
}

DEFINE_PROFILE(free_stream_profile,t,i)
{
real x[ND_ND];      /* this will hold the position vector */
real y;
face_t f;
begin_f_loop(f,t)
{
F_PROFILE(x,f,t);
y=x[1]+0.165;
if (y < 3.600)
F_PROFILE(f,t,i) = (29.1/3400)*(y*1000-200)+295.9+273.15;

else if (y < 4.000)
F_PROFILE(f,t,i) = (3/400)*(y*1000-3600)+325+273.15;

else if (y < 4.300)
F_PROFILE(f,t,i) = 0.005*(y*1000-4000)+328+273.15;

else
F_PROFILE(f,t,i) = 329.5+273.15;
}
end_f_loop(f,t)
}

```